View metadata, citation and similar papers at core.ac.uk
brought to you by CORE
provided by Aaltodoc Publication Archive

HELSINKI INSTITUTE OF PHYSICS INTERNAL REPORT SERIES

HIP-2008-07

PROCESSING OF RADIATION HARD PARTICLE DETECTORS ON CZOCHRALSKI SILICON

Esa Tuovinen
Helsinki Institute of Physics
P.O.Box 64, FI-00014 University of Helsinki, Finland

Dissertation for the degree of Doctor of Science in Technology to be presented with due permission of the Faculty of Electronics, Communication, and Automation for public examination and debate in Large Seminar Hall (2190) of Micronova at Helsinki University of Technology (Espoo, Finland) on the 31th of October, 2008, at 12 noon.

Espoo 2008

ABSTRACT OF DOCTORAL DISSERTATION	HELSINKI UNIVERSITY OF TECHNOLOGY P.O. BOX 1000, FI-02015 TKK http://www.tkk.fi
Author	
Name of the dissertation	
Manuscript submitted	Manuscript revised
Date of the defence	
Monograph	Article dissertation (summary + original articles)
Faculty Department Field of research Opponent(s) Supervisor Instructor	
Abstract	
Keywords	
ISBN (printed)	ISSN (printed)
ISBN (pdf)	ISSN (pdf)
Language	Number of pages
Publisher	
Print distribution	
The dissertation can be read at http://lib.tkk.fi/Diss/	

VÄITÖSKIRJAN TIIVISTELMÄ	TEKNILLINEN KORKEAKOULU PL 1000, 02015 TKK http://www.tkk.fi
Tekijä	
Väitöskirjan nimi	
Käsikirjoituksen päivämäärä	Korjatun käsikirjoituksen päivämäärä
Väitöstilaisuuden ajankohta	
Monografia	Yhdistelmäväitöskirja (yhteenveto + erillisartikkelit)
Tiedekunta Laitos Tutkimusala Vastaväittäjä(t) Työn valvoja Työn ohjaaja	
Tiivistelmä	
Asiasanat	
ISBN (painettu)	ISSN (painettu)
ISBN (pdf)	ISSN (pdf)
Kieli	Sivumäärä
Julkaisija	
Painetun väitöskirjan jakelu	
Luettavissa verkossa osoitteessa http://lib.tkk.fi/Diss/	

Acknowledgements

The research for this thesis was carried out during the years 2003-2007 in the Helsinki Institute of Physics CMS Tracker Project. Most of the work on my part was done at the Helsinki University of Technology Micro and Nanofabrication Center. Many of the tasks included were performed at CERN or in collaboration with other institutes. Irradiations were done at CERN or at the Jyväskylä University Accelerator Laboratory. In addition to the electrical characterization done at the CERN Solid State Detector Laboratory, some of the measurements were done at the Brookhaven National Laboratory, the Ioffe Institute, and at the Lappeenranta University of Technology.

I would like to thank Docent Sami Franssila for supervising my studies. I would like to thank the pre-examiners, Simo Eränen and Heikki Sipilä, for their valuable comments.

I am grateful to Professor Jorma Tuominiemi for giving me the opportunity to work at this fine institute. I would like to thank Dr. Eija Tuominen for all her support and always pushing me to work harder. I would also like to thank my instructor Dr. Jaakko Härkönen for all the interesting discussions and for always keeping me busy with the process development.

I would like to thank Väisälä Foundation, Jenny and Antti Wihuri Foundation, and Waldemar von Frenckell Foundation for supporting my research.

I would like to thank all my colleagues at CERN, Helsinki University of Technology and at other institutes. Without them this work could not have been done.

I would like to thank all my personal friends and family for all their support and friendship.

Finally, I would like to thank Janna for all her love and support.

Espoo, September 17th, 2008.

Esa Tuovinen

List of publications

1. E. Tuovinen, J. Härkönen, P. Luukka, E. Tuominen, *Intentional thermal donor activation in Magnetic Czochralski silicon*, Materials Science in Semiconductor Processing 10 (2007) 179-184.

2. E. Tuovinen, J. Härkönen, P. Luukka, E. Tuominen, E. Verbitskaya, V. Eremin, I. Ilyashenko, A. Pirojenko, I. Riihimäki, A. Virtanen, K. Leinonen, *Czochralski silicon detectors irradiated with 24 GeV/c and 10 MeV protons*, Nuclear Instruments and Methods in Physics Research A 568 (2006) 83-88.

3. J. Härkönen, E. Tuovinen, Z. Li, P. Luukka, E. Verbitskaya, V. Eremin, *Recombination Lifetime Characterization and Mapping of Silicon Wafers and Detectors Using the Microwave Photoconductivity Decay (μPCD) Technique*, Materials Science in Semiconductor Processing 9 (2006) 261-265.

4. J. Härkönen, E. Tuovinen, P. Luukka, H.K. Nordlund and E. Tuominen, *Magnetic Czochralski silicon as detector material*, Nuclear Instruments and Methods in Physics Research A579 (2007) 648-652.

5. J. Härkönen, E. Tuovinen, P. Luukka, E. Tuominen, and Z. Li, *$p^+/n^-/n^+$ Cz-Si Detectors Processed on p-Type Boron-Doped Substrates With Thermal Donor Induced Space Charge Sign Inversion*, IEEE Transactions on Nuclear Science 52 (2005) 1865-1868.

6. J. Härkönen, E. Tuovinen, P. Luukka, E. Tuominen, Z. Li, A. Ivanov, E. Verbitskaya, V. Eremin, A. Pirojenko, I. Riihimki and A. Virtanen., *Particle detectors made of high-resistivity Czochralski silicon*, Nuclear Instruments and Methods in Physics Research A 541 (2005) 202-207.

Author's contribution

This research was carried out at the Helsinki Institute of Physics within the CMS Tracker group and in the framework of the CERN RD50 and RD39 collaborations during the years 2004-2007. During this time, the author was in charge of the device processing and process development and participated in the device characterization and irradiations presented in this thesis. The publications in this thesis are a result of a group effort. The author is the main writer in Publications 1 and 2. In Publication 3, the author processed all the samples and made all the characterization measurements. In Publication 4, in addition to the processing of the samples, the author participated in the CV and IV characterization and made all the thermal donor tests. In Publication 5, the author has been in charge of processing and thermal donor generation tests. In Publication 6, the author processed all the detectors and participated in the low-energy proton irradiations. The results of the publications have also been presented at international conferences.

Summary of publications

1. Intentional thermal donor activation in Magnetic Czochralski silicon

This paper presents a quantitative study about the thermal activation of thermal donors in high-resistivity magnetic Czochralski silicon. The thermal donor activation was performed through a thermal treatment at 430°C up to a total time of 80 min. The space charge density after each annealing step was extracted from Capacitance-Voltage (CV) measurements. We improved the previously reported model of thermal donor generation.

2. Czochralski silicon detectors irradiated with 24 GeV/c and 10 MeV protons

This paper presents the studies conducted on pad detectors after proton irradiation. Samples were characterized with CV measurements, the Transient Current Technique (TCT) and voltage potential measurements with a Scanning Electron Microscope (SEM). We present the evolution of the effective doping concentration as a function of irradiation fluence, as well as the introduction rate of the negative space charge, the β-parameter. MCz-Si was found to be more radiation-hard than FZ-Si. Both TCT and SEM measurements were used to investigate the possible Space Charge Sign Inversion (SCSI).

3. Recombination Lifetime Characterization and Mapping of Silicon Wafers and Detectors Using the Microwave Photoconductivity Decay (μPCD) Technique

This paper describes the application of recombination lifetime measurements by the

microwave photoconductivity decay (μPCD) technique on oxidized high-resistivity silicon. The recombination lifetime is a measure of the material quality, i.e., defect/impurity concentration, which affects the quality of the resulting detectors and their electrical properties. In general, the recombination lifetime is the smallest around the wafer edges (about 1-2 ms), and highest in the center of the wafer (5-10 ms). The recombination lifetime was measured under different injection levels and surface charge conditions. MCz-Si wafers were found to be an excellent starting material for detector applications.

4. Magnetic Czochralski silicon as detector material

This paper presents a brief overview of the Czochralski crystal growth technique. The device fabrication process issues of Cz-Si are discussed and the formation of thermal donors is especially emphasized. $n^+/p^-/p^+$ and $p^+/n^-/n^+$ detectors were processed on magnetic Czochralski (MCz-Si) wafers. Capacitance Voltage (CV) and Current voltage (IV) data of AC-coupled strip detectors are presented. The paper also presents data from pad detectors, as well as the experimental results of intentional TD doping. Data on the spatial homogeneity of electrical properties, full depletion voltage, and leakage current are shown to be sufficient and n and p-type devices are compared. Our results show that it is possible to manufacture high-quality particle detectors from high-resistivity Cz-Si.

5. $p^+/n^-/n^+$ Cz-Si Detectors Processed on p-Type Boron-Doped Substrates With Thermal Donor Induced Space Charge Sign Inversion

This paper presents a process for fabricating detectors on p-type wafers with intentional thermal donor-induced SCSI. The detector processing was carried out using the common procedure for standard n-type wafers. During the last process step, i.e. the sintering of the aluminum electrode, the p-type bulk was turned to n-type through the generation of thermal donors (TD). The full depletion voltage of the detectors could be tailored over a wide range (30 to 1000 V). The SCSI in the TD-generated devices was verified by transient current technique measurements. The detectors show a very small increase of full depletion voltage, i.e. excellent radiation hardness, after irradiations with 24 GeV/c protons.

6. Particle detectors made of high-resistivity Czochralski silicon

This paper describes our pin-diode and strip detector process for Czochralski silicon wafers. The oxygen level in high-resistivity Czochralski silicon is optimal for semiconductor fabrication, as well as for radiation hardness. The radiation hardness of the devices was investigated with irradiations with low- and high-energy protons, neu-

trons, γ-rays, lithium ions, and electrons. Cz-Si was found to be more radiation-hard than standard FZ-Si or oxygenated FZ-Si.

Contents

Acknowledgements **vii**

List of publications **ix**
Author's contribution . . . x
Summary of publications . . . x

Contents **xiii**

1 Introduction **1**

2 Operation of particle detectors **3**
2.1 Theory of p-n junction . . . 3
2.2 The operation of silicon strip detectors . . . 7

3 Czochralski silicon **9**
3.1 Czochralski silicon growth method . . . 9
3.2 Impurities in Czochralski silicon . . . 10
3.3 Thermal donors in Czochralski silicon . . . 11

4 Processing of MCz strip detectors **13**
4.1 Detector layout . . . 13
4.2 Process flow . . . 14
4.3 Detector process on p-type wafers . . . 19
4.4 Thermal donor compensation . . . 19
4.5 Process characterization . . . 21

5 Radiation hardness of silicon detectors **27**
5.1 NIEL scaling hypothesis . . . 27
5.2 Radiation effects in silicon detectors . . . 28
5.3 Effect of oxygen on radiation hardness . . . 33
5.4 Advantages of p-type detectors . . . 34

5.5 Characterization of detectors 34

6 Conclusions **41**

Bibliography **43**

A Full process flow **47**

List of Symbols **51**

List of Abbreviations **53**

Chapter 1

Introduction

Silicon detectors in high-energy physics (HEP) experiments are exposed to a very hostile radiation environment. A possible upgrade of the luminosity of the CERN LHC (Large Hadron Collider) up to 10^{35} cm^{-2}s^{-1} has been proposed. This would raise the fluencies of fast hadrons up to 10^{16} cm^{-2}, well beyond the operational limits of present silicon detectors.

Particle radiation causes irreversible crystallographic defects in silicon material, leading to drastic effects on the performance of the detector. The increased concentration of generation-recombination centers results in an increased detector leakage current. Additionally, some of the defects compensate the initial doping concentration of the silicon, which leads to changes in operating voltages [1]. Ultimately, the degradation of the charge-collection efficiency (CCE) caused by the trapping of charge carriers will severely limit the performance of the detector.

Many approaches to this problem have been investigated, including e.g. the defect engineering of the bulk material [1], using p-type material or epi material, using other more exotic materials (e.g. SiC or diamond) [2, 3], operating the devices at a cryogenic temperature in a reverse or a forward-biased mode (Current Injected Detectors, CID) [4, 5, 6], and designing special detector geometries (e.g. 3D) [2].

The sensors used in particle tracking systems must be fully depleted at a reasonably low operating voltage. A practical limit for the operating voltage is 500 volts. Detectors have traditionally been fabricated on silicon wafers manufactured by the float-zone growth technique [7]. The float-zone technique ensures the growth of high-purity and sufficiently defect-free silicon crystals that are basic requirements for high-resistivity substrates for detector applications [8]. On the other hand, float-zone silicon (FZ-Si) characteristically has a low oxygen concentration as a result of the contactless crystal growth technique. However, the low oxygen concentration is a drawback since oxygen has been found to improve the radiation hardness of silicon detectors, as demonstrated by the the CERN-RD48 collaboration [1, 9].

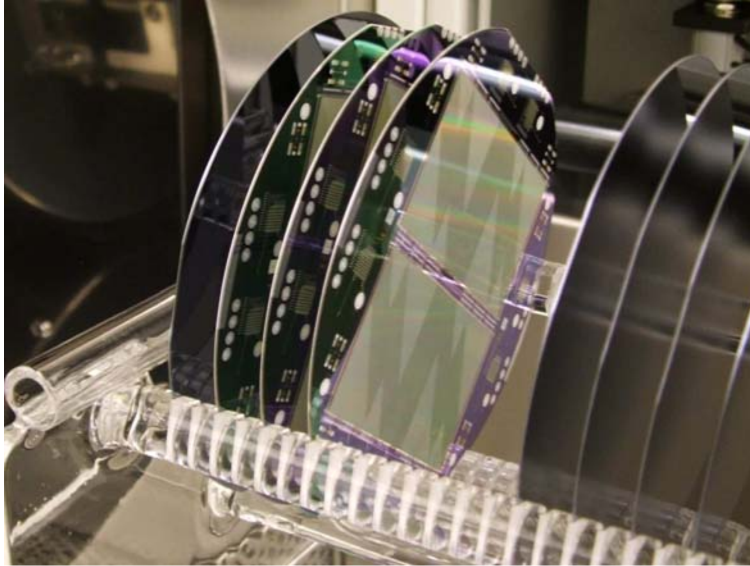

Figure 1.1: Finished silicon particle detectors.

The Czochralski crystal growth method enables silicon wafers with sufficiently high resistivity and a well-controlled oxygen concentration to be produced [10]. Although Czochralski silicon (Cz-Si) is the basic raw material for the microelectronics industry, high-resistivity (>1 kΩcm) Cz-Si wafers suitable for detector fabrication have only been available for a few years. This is probably due to the lack of commercial applications in which both high-resistivity and tailored oxygen concentrations are required. The first "detector-grade" wafers were actually processed for power electronics applications.

An additional benefit of using Cz-Si is the possibility of tailoring the depletion voltages of the processed detectors. During elevated annealing processes, so-called Thermal Donors (TDs) can be introduced into the silicon bulk. Because of the low doping concentration in the silicon, the concentration of the TDs can be comparable to the initial doping concentration. This kind of tailoring is mainly beneficial for detectors made of p-type material. In p-type Cz-Si, this leads to increased resistivity and even type-inversion, from p-type material to n-type material. In n-type Cz-Si, thermal donors increase the overall doping concentration, thus reducing resistivity.

In this thesis work I have studied detector fabrication processes on Czochralski silicon, the potential of thermal donors for detector processes, and the radiation hardness properties of our detectors investigated by a selection of characterization techniques. Figure 1.1 shows wafers after the final furnace annealing step. After annealing the wafers are ready for dicing. This thesis is organized as follows. First, the basic theory of the operation of particle detectors is presented. Next, the properties of the Czochralski silicon material and the processing of the strip detectors are described. Finally, the radiation hardness of the detectors is discussed.

Chapter 2

Operation of particle detectors

A silicon particle detector is usually a reverse-biased p-n junction. When biased, the electric field extends from the junction to the opposite side of the detector. When electron-hole pairs (ehps) are created in the field region, they are separated and collected from the opposite sides of the detector. Usually one, or, in some cases, both sides of the detector are segmented in order to get positional data out of the device.

2.1 Theory of p-n junction

The well-established theory presented in this section is based on reference [11].

The formation of a p-n junction can be thought to occur when regions of p- and n-type silicon are brought into contact. Holes diffuse from the p-region to the n-region and recombine there, leaving behind negatively charged acceptor states near the junction. Similarly, electrons diffuse from the n-region, leaving behind positively charged donor states. A region depleted of free charge carriers is created on both sides of the junction. This region is also called the depletion region. An electric field, related to the amount of ionized charge carriers, is created. The drift current induced by this field compensates the diffusion current related to the charge carrier density gradient. Figure (2.1) illustrates the properties of such an ideal p-n junction.

Electric field and potential distribution

A real p-n junction is often approximated by an abrupt junction, where the net dopant density changes stepwise from the acceptor atom density, N_A, to the donor density, N_D. By applying Poisson's equation in thermal equilibrium in the n-region and the p-region in one dimension, x, we get:

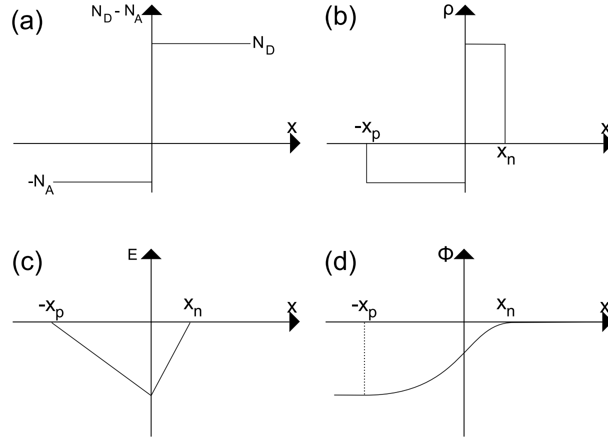

Figure 2.1: Abrupt p-n junction in thermal equilibrium: (a) net dopant densities; (b) space charge; (c) electric field, and (d) potential distributions. The abbreviations will be explained later in this chapter.

$$\frac{dE}{dx} = -\frac{d^2\phi}{dx^2} = \frac{\rho}{\epsilon_s} = \frac{qN_D}{\epsilon_s} \qquad \text{and} \tag{2.1}$$

$$\frac{dE}{dx} = -\frac{d^2\phi}{dx^2} = \frac{\rho}{\epsilon_s} = -\frac{qN_A}{\epsilon_s} \qquad , \tag{2.2}$$

where E is the electric field, ϕ the electric potential, ρ the space-charge density, ϵ_s the permittivity of the semiconductor, and q the absolute value of the electron charge. For the sake of clarity, the equations are presented only for the n-region. By applying boundary conditions $E(x = x_n) = 0$ in the n-region and integrating we get:

$$E = \frac{qN_D}{\epsilon_s}(x - x_n) \qquad , \qquad 0 < x < x_n \tag{2.3}$$

The electric field depends linearly on x and has a maximum, E_{max}, at the p-n interface where $x = 0$

$$E_{max} = |E(x = 0)| = \frac{qN_D}{\epsilon_s}x_n \qquad . \tag{2.4}$$

To get the potential across the junction, we integrate once more with the boundary condition $\phi(x = x_n) = 0$:

$$\phi(x) = -\frac{qN_D}{2\epsilon_s}(x - x_n)^2, \qquad 0 < x < x_n \qquad . \tag{2.5}$$

The built-in potential can be derived from Equation (2.4):

$$V_{bi} = \frac{1}{2}E_{max}(x_n + x_p) = \frac{1}{2}E_{max}W \qquad , \tag{2.6}$$

where x_n and x_p are the width of the depletion region in the n- and p-regions, respectively, W is the width of the whole depletion region. By eliminating E_{max} from Equations (2.4) and (2.6) we get:

$$W = \sqrt{\frac{2\epsilon_s}{q}(\frac{N_A + N_D}{N_A N_D})V_{bi}} \tag{2.7}$$

In the case of a one-sided junction $N_A \gg N_D$ Equation (2.7) can be simplified to

$$W \approx \sqrt{\frac{2\epsilon_s V_{bi}}{qN_B}} \quad , \tag{2.8}$$

where N_B is the doping density in the lightly doped bulk material. Even though the junction spreads strongly to the weakly doped side, it also extends to the other side. For a typical detector material, the effective bulk doping is less than 10^{13} cm^{-3} and the dopant concentration in the heavily doped region is greater than 10^{18} cm^{-3}. In such a case, the junction spreads only a few nanometers to the heavily doped side.

External biasing

Now we consider the effects of applying external bias voltage to the device. We assume that no voltage drop is seen as a result of ohmic contact resistance and that the bias voltage is spread across the whole p-n junction. The voltage drop in the diode is $V_{bi} - V_{ext}$ where V_{ext} is the external bias voltage. Equation (2.8) can be expressed as:

$$W \approx \sqrt{\frac{2\epsilon_s}{qN_B}(V_{bi} - V_{ext})} \tag{2.9}$$

In a typical detector structure the bulk acts as a detecting volume. Therefore, it is beneficial to deplete the whole substrate thickness, if possible. This depletion voltage is also often referred to as the operation voltage of the detector. It is desirable to operate the detector at a relatively low bias voltage level. From Equation (2.9) we can see that this can be realized through wafer selection, by choosing a thinner substrate or a higher-resistivity substrate, or it can sometimes be adjusted during processing by varying process parameters.

Leakage current in reverse-biased detector

In an ideal p-n diode, the leakage current is dominated by the diffusion current and the current density can be approximated by the Shockley equation:

$$J_S = \frac{qD_p p_{n0}}{L_p} + \frac{qD_n n_{p0}}{L_n} \quad , \tag{2.10}$$

where D_p and D_n are the diffusion coefficients for holes and electrons, p_{n0} and n_{p0} the minority carrier densities in the equilibrium case and L_p and L_n the diffusion lengths for holes and electrons, respectively.

In a real diode, the leakage current is a combination of the surface recombination current, the generation current in the depletion region, and the ideal-case diffusion current. The surface recombination current is usually effectively suppressed by a proper surface passivation.

Next, we consider the effect of bulk carrier generation on current density, J_{gen} given by [11]:

$$J_{gen} = \frac{qn_iW}{\tau_G} \quad , \tag{2.11}$$

where n_i is the intrinsic charge carrier concentration, W is the width of the depletion layer, and τ_G is the generation lifetime. The generation lifetime is considered to have the same temperature dependence as n_i. In the case of an abrupt p-n junction:

$$J_{gen} \propto \sqrt{V_{bi} - V_{ext}} \tag{2.12}$$

For detector-grade silicon material, we find that the carrier generation current is the predominant term in the leakage current in the reverse-biased mode and the total current can be approximated with Equation (2.11).

Junction breakdown

Junction breakdown sets the limit to how much we can increase the reverse bias voltage. There are two mechanisms for junction breakdown in silicon.

In Zener breakdown, a high electric field causes quantum mechanical electron tunneling to create electron-hole pairs (ehps), which in turn contribute to the junction current. The probability of electron tunneling starts to be significant when the electric field approaches 10^6 V/cm [11]. Obtaining such a field in a p^+n detector structure is usually impossible.

In avalanche breakdown, a high electric field gives the charge carriers enough energy to create new ehps when colliding with the lattice. Every such collision creates two new charge carriers that can continue the process, increasing the junction leakage current drastically. In the case of avalanche breakdown, for an abrupt one sided p-n junction the breakdown voltage, V_B, can be approximated by [11]:

$$V_B = \frac{E_BW}{2} = \frac{\epsilon_s {E_B}^2}{2qN_B} \quad , \tag{2.13}$$

where E_B is the critical value for the electric field causing the breakdown, W the width of the depletion region, and N_B is the doping concentration in the lightly doped bulk material. For normal detector bulk material, the breakdown voltage is much larger than the bias voltage obtainable from regular source meter units (SMUs).

Thus we can conclude that the possible breakdown in a real device arises from the device geometry.

Junction capacitance in a reverse-biased diode

We can derive the expression for the p-n junction capacitance using the same approximations as used in solving Poisson's equation. The general expression for small-signal capacitance per unit area, C, is [11]:

$$C = \frac{\epsilon_s}{W} \tag{2.14}$$

Combining Equations (2.9) and (2.14) we get

$$C = \sqrt{\frac{q\epsilon_s N_B}{2(V_{bi} - V_{ext})}} \quad . \tag{2.15}$$

From Equation (2.15) we can see that before depletion, the capacitance is inversely proportional to the square root of the external reverse bias voltage, V_{ext}, and at full depletion it reaches the minimum value of:

$$C_{geo} = \frac{\epsilon_s A}{d} \quad , \tag{2.16}$$

where A is the area of the diode and d is the thickness of the diode. This is also called the geometrical capacitance, because it only depends on the size of the diode junction. From the full depletion voltage data, extracted from the CV measurements, it is possible to extract approximate values for the effective doping concentration in the silicon bulk.

2.2 The operation of silicon strip detectors

In a particle detector structure based on a p-n junction, the diffusions are traditionally formed on the opposite sides of the wafer, i.e. p$^+$ strips are implanted on the front surface and the n$^+$ region on the back of the wafer. Therefore, when biased, the whole bulk of the wafer acts as a detecting volume. Figure 2.2 presents the space charge region in an unbiased and in a reverse-biased detector. Electric field spreads from the p$^+$ region to the n$^+$ region. After full depletion, the strength of the electric field continues to grow until saturation.

In modern high-energy physics experiments, event rates are quite high, e.g. the time between different events is of the order of a few tens of nanoseconds. Therefore, diffusion is too slow a method for collecting the signal charge. The whole bulk is depleted by reverse bias voltage and the charge is collected from the drifting carriers. In a typical 300-μm-thick detector, the electrons are collected within about 10 ns and holes within about 25 ns.

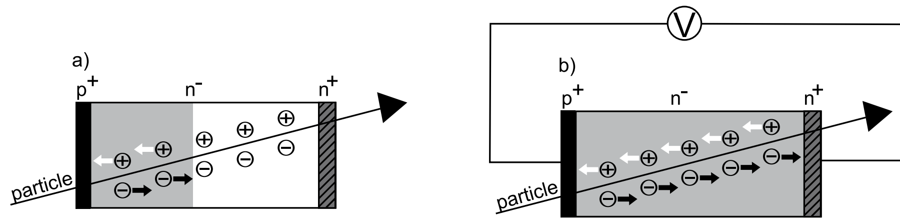

Figure 2.2: (a) unbiased detector and (b) fully depleted detector (Picture by H. Viljanen).

When a particle hits such a detector, it creates ehps in the bulk which in turn are separated in the electric field. Holes and electrons drift to the opposite contacts and are measured with read-out electronics. The small ionizing energy of silicon makes it a good detector material. The average energy used to create ehp in silicon is 3.67 eV [12]. The energy band-gap of silicon at room temperature is 1.12 eV. The remaining part of the energy goes to lattice vibrations and other reactions. For mips, the most probable charge deposition in a 300-μm-thick silicon detector is about 22,000 electrons [12].

Modern detectors used in HEP experiments are AC-coupled. Traditional DC-coupled detectors have their read-out electronics connected directly to a strip implant. The drawback with DC-connected detectors is that the leakage current is also connected to the read-out electronics. In an AC-coupled detector, the signal current is separated from the leakage current on the detector wafer by reading the signal through a simple high-pass filter. The signal current is read through a strip capacitor and the leakage current goes through the bias resistor to the common bias line.

The signal level in a fully depleted unirradiated detector depends solely on the wafer thickness. In order to increase the signal level, a thicker substrate would be required. A thicker wafer requires a higher operation voltage, since $V_{dep} \propto W^2$. This contradiction leads to a compromise between signal level and operation voltage. Additionally, the operation voltage changes as the detector is exposed to radiation, as will be explained in Chapter 5. In order to ensure acceptable detector performance, this change has to be taken into account when selecting the detector wafers and the process parameters.

Chapter 3

Czochralski silicon

Czochralski silicon is the most widely used silicon growth method in the world, with a market share of over 95% [13]. The remaining 5% is float-zone silicon. Traditionally, in the high-energy physics (HEP) community, float-zone silicon (FZ-Si) has been used because of its high resistivity and purity [7]. The downsides of FZ-Si are its low oxygen concentration (radiation hardness) and wafer size limitation (150-mm wafers). Historically, FZ-Si has been widely used in the HEP community and because of this fact, Czochralski silicon has been mistaken for something new. What is new in Cz-Si is the availability of high-resistivity material.

3.1 Czochralski silicon growth method

In the CZ method [10], illustrated in Figure 3.1, a fused silica crucible located in a furnace is filled with electronic-grade polysilicon (EGS). The desired dopant atoms are added either as doped silicon pieces or in an elemental form. Then the mixture is melted in an inert atmosphere, e.g. an argon atmosphere. A small seed crystal of a known orientation is dipped into the silicon melt. The seed crystal is quickly drawn from the melt in order to suppress dislocations originating from the temperature gradient between the seed crystal and the melt. A fast initial pull rate results in the formation of a thin neck in to the crystal. Then the pull rate is reduced. All the time, the forming silicon ingot and the silica crucible are rotated, usually in opposite directions. The ingot copies the orientation from the seed crystal.

MCz-Si is essentially very similar to regular Czochralski silicon. The main difference is that a strong magnetic field is present during the growth of the ingot, since the silicon melt is a conducting liquid and the movement of the melt can be influenced by the magnetic field [14]. This in turn affects the concentrations and distributions of impurities inside the forming ingot.

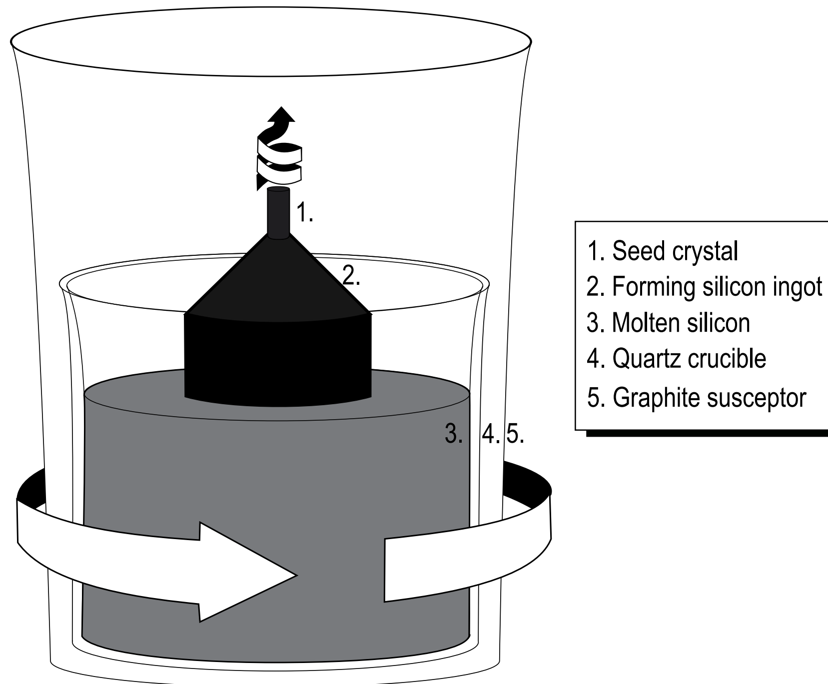

Figure 3.1: Czochralski silicon growth method (Picture by H. Viljanen).

3.2 Impurities in Czochralski silicon

During the growth of the crystal, the silica crucible is gradually dissolved into the silicon melt. This process releases impurities and dopants, namely oxygen, carbon, aluminum, and boron. Most of the oxygen vaporizes as silicon monoxide and is flushed away by the argon gas flow, but some of it stays in the melt and is incorporated into the forming crystal. Other impurities are not flushed away and stay in the melt. Fortunately, the solubilities of impurities and dopant atoms are greater in the molten form than in the solid form. Thus, the forming crystal is more pure than the silicon melt as a result of the segregation of impurity atoms. Typical concentrations for carbon and oxygen for different growth methods are listed in Table 3.1. The impurity concentrations in the Table 3.1 are from Reference [7]. The most important difference for radiation detector use is the higher oxygen concentration in Cz and MCz silicon, combined with the sufficient resistivity in the MCz-Si. The prices are for high-resistivity silicon and are strongly affected by the low supply and demand. The 10-cm FZ-Si and MCz-Si wafers used in scientific research cost practically the same, roughly 50€ each.

Table 3.1: List of typical values for different silicon materials: impurity concentrations are typically lower for FZ-Si [7].

	FZ	Cz	MCz
Max. Resistivity	30 kΩcm	500 Ωcm	2 kΩcm
Min. Doping [cm^{-3}]	$< 10^{12}$	10^{13}	5×10^{12}
O [cm^{-3}]	$< 10^{16}$	10^{18}	5×10^{17}
C [cm^{-3}]	$< 10^{16}$	10^{16}	
Wafer diameter [mm]	≤ 150	≤ 300	

3.3 Thermal donors in Czochralski silicon

It is well known that the aggregation of oxygen atoms leads to formation of electrically active defects, commonly named thermal donors (TD) [15, 16]. TDs are among the most studied defects in semiconductors. The TDs are shallow donor levels below the conduction band [17]. The formation of thermal donors depends strongly on the temperature and the oxygen concentration in the silicon material. For the generation of roughly 10^{13} TDs in a cubic centimeter in an hour, an interstitial oxygen concentration in excess of 10^{17}cm^{-3} is required. In high-resistivity silicon, heat treatment between 400–600°C can yield a TD concentration comparable with the initial doping concentration. The formation of TDs has often been explained as being due to so-called anomalously fast diffusing species (FDS). It has been proposed that oxygen dimers (O2) and trimers (O3), among other oxygen complexes, are such FDSs [18]. However, more recent studies have shown that the kinetics of TD formation is dominated by the capturing or escaping of interstitial oxygen by diffusing oxygen chains [19]. The molecular structure of two thermal donors is presented in Figure 3.2, according to Reference [20].

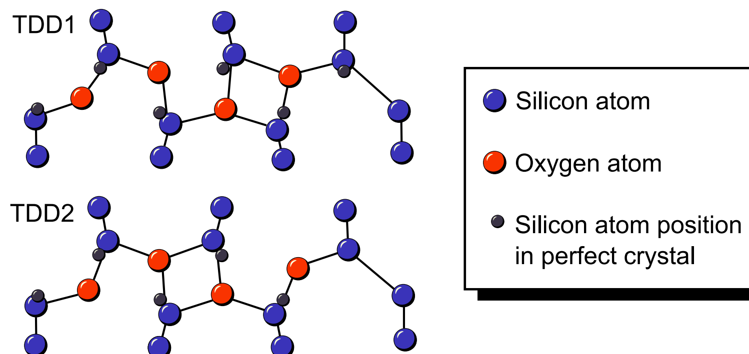

Figure 3.2: Molecular structure of thermal double donors, TDD1 and TDD2.

The formation of TDs starts approximately at a temperature of approximately 400°C. The introduction rate is strongly dependent on the temperature, i.e. an increase of 50°C leads to a much greater generation rate. As the temperature increases more, new TD levels start to form. If the temperature increases to over 700°C, all existing TDs will be annihilated. This phenomenon can be used to keep the initial level of thermal donors under control, i.e. all the TDs are annihilated during a high-temperature oxidation step and if the pull-out is done at a high enough temperature and in a fast manner, unwanted TD generation can be kept to a minimum level.

Usually, TDs are considered to be unwanted defects. If the oxygen concentration has large variations, the concentration of TDs will vary, resulting in variance in device properties. Furthermore, in the case of Cz-Si, TD generation limits the controllably attainable resistivity to moderate values, i.e. to a few kΩcm. When combined with high-resistivity MCz-Si, TDs can be used to tailor device parameters over a wide range.

Chapter 4

Processing of MCz strip detectors

In this chapter I will describe in detail our strip detector process. The process has gone through many changes over the years and only the latest version is described. Our previous processes have also been described, in References [21, 22]. Later on, I will concentrate on various process characterization methods and their application in detector characterization. The full process flow is included in Appendix A.

4.1 Detector layout

The main structures in our detectors, shown in Figure 4.1, are guard rings, bias line, bias resistors, strip implants, and strip capacitors. These structures can be further divided into an active region and guard rings. Usually, during operation, the high voltage is connected to the contact at the back and the contacts on the front surface are connected to the ground.

The AC-coupled detector is in fact a simple high-pass filter in itself. The signal is read through strip capacitors and the strips are separated from each other with bias resistors. The bias resistors are connected at one end to the strip implant and at the other end to the common bias line. The bias line is usually grounded.

The active region is surrounded by guard rings. In our current design, we have one wide guard ring that is grounded during operation and 16 floating guard rings. If a high-voltage is connected to the edge of the front surface, the electric field is divided between these rings and electrical breakdown can be avoided.

In order to prevent breakdown in the active region, various measures have been taken. All metallizations extend over the field oxide layer. These overhangs help in avoiding strong electric fields and breakdowns near the edges of the lines. In order to avoid sharp peaks in the electric field, all the ends of the implants and metallizations are rounded. For the same reason, the implants are diffused for a relatively long time,

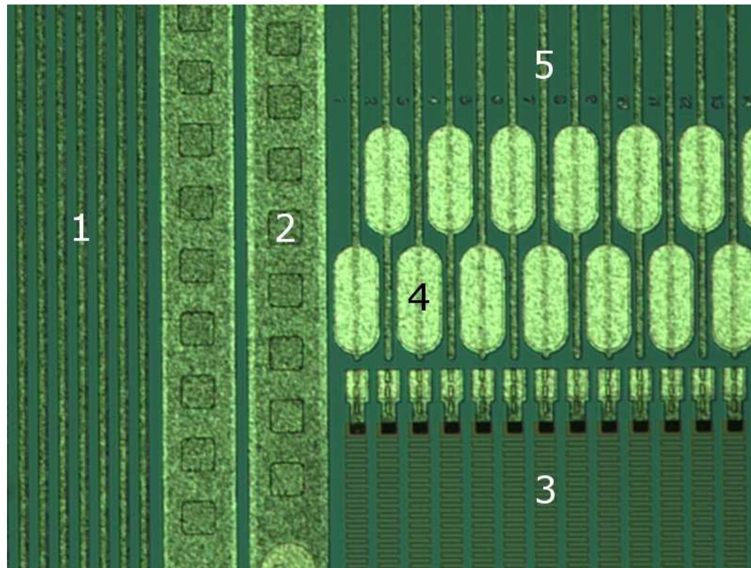

Figure 4.1: The features of the strip detector layout: 1) guard rings (16 narrow + 1 wide); 2) bias line; 3) bias resistors; 4) bonding pads, and 5) strip capacitors. Contact openings can be seen as lighter areas.

resulting in deep and smooth implantation profiles.

For research purposes, we have also processed pad detectors. Pad detectors are non-segmented diodes with an active area of 5 mm $\times$ 5 mm surrounded by the same guard ring structure as the strip detectors. The process is essentially the same, except that the bias resistor deposition and patterning steps are omitted. Our current strip detector mask set produces two big strip detectors, 12 mini-strip detectors, and 24 small pad detectors from a single wafer.

4.2 Process flow

All the processing was done at the Micro- and Nanofabrication Center (MINFAB) of Helsinki University Technology (TKK) [23]. MINFAB has roughly 700 square meters of class 100/10 cleanroom space. The process equipment includes oxidation furnaces, 1$\times$ contact/proximity lithography, ion implantation, sputtering, atomic layer deposition, two reactive ion etchers (RIE), regular and cryo ICP-RIE, plasma-enhanced chemical vapor deposition (PECVD), and various wet benches and fume hoods for wet chemical processing. The process flow is illustrated in Figure 4.2. The process steps go from the top down and from left to right, with the latest layer specified in the picture.

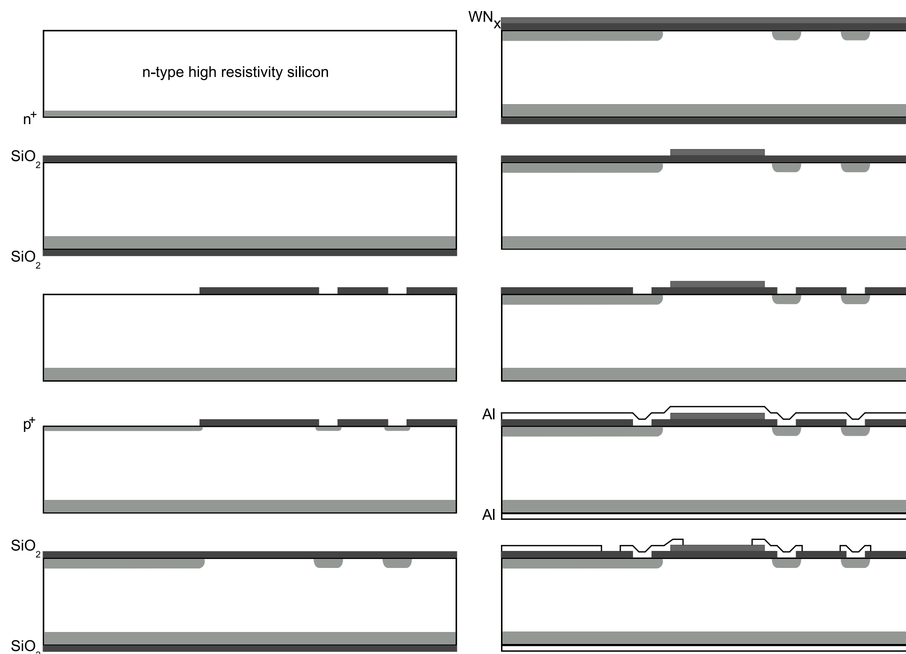

Figure 4.2: Process flow for the n-type strip detectors. Process steps from top to bottom, left to right: implantation of the back surface, implantation mask oxidation, implantation mask patterning, front side implantation, field-oxide oxidation, tungsten nitride (WN_x) sputtering, WN_x patterning, implant contact openings, aluminum sputtering, and aluminum patterning. For pad detectors, omit tungsten nitride deposition and patterning.

Implantation of the back surface

Our current process starts with back surface ion implantation. This implantation is not patterned and therefore, because of the lack of lateral diffusion, implants can be diffused deeper into the silicon. The amorphization dose for 70 keV phosphorus implantation is 6×10^{14} (ICECREM 4.3) and therefore the implantation region, roughly 200 nm from the surface, is heavily damaged. In our process this damaged layer and strong implantation are used as a gettering region for impurities.

Implantation mask oxidation

Prior to masking oxidation, the wafers are thoroughly cleaned with RCA cleaning. The name comes from the company name behind this invention, the Radio Corporation of America. The cleaning sequence consists of the removal of organics and particles in a heated ammonium hydroxide - hydrogen peroxide bath, the removal of metallics in a heated hydrogen chloride - hydrogen peroxide bath and the removal of chemical oxide in a diluted hydrogen fluoride bath. The masking oxide layer is grown in a Centrotherm furnace at a temperature of 1100°C. The oxidation takes ap-

proximately 300 minutes in a dry-oxygen atmosphere and results in a 300-nm oxide layer. The degradation of the minority carrier lifetime during oxidation is regularly monitored with the Microwave Detected Photoconductivity Decay method (μPCD). See. Section (4.5) for further details.

Patterning of alignment marks

After this oxidation, alignment marks, to be used in the following mask layers, are patterned with lithography. A typical photolithography step includes heating in an oven at 120℃, priming with 1,1,1,3,3,3-hexamethyldisilazane (HMDS) in a vacuum exicator, resist spinning, pre-baking at 90℃, exposure, development, and post-baking at 120℃. Patterned marks are then etched about 0.5 μm deep into the silicon with a reactive ion etcher (RIE). The etching is done in a two-step process consisting of oxide etching and bulk silicon etching. After etching, the resist layer is removed with acetone + ultrasound, fresh acetone, and iso-propanol.

Formation of p^+ implants

The p^+ regions are formed using ion implantation. Prior to implantation, the oxide layer is patterned with lithography and a subsequent buffered hydrogen fluoride (BHF) etch. Before implantation, the remaining resist mask is removed. The patterned wafers are implanted with an Eaton ion implanter with 30 keV Boron ions to a total dose of 10^{15} ions/cm^2. The simulated range for 30 keV boron ions is 119 nm (SRIM 2008), but because of the very low bulk doping concentration we need to have 300 nm of masking oxide in order to ensure that very few boron atoms are implanted through the mask oxide. The ion implantation simulation results are presented in Section 4.5. After implantation, the remaining implantation mask is removed and new field oxide is grown. The oxidation is again started with RCA clean and a 100 nm or 200 nm oxide layer is grown at a temperature of either 1100℃ or 1050℃. During this oxidation, even the heavier lattice damage caused by the ion implantation is thoroughly annealed and the implants are diffused to their final depths of approximately 3.5 μm and 7 μm for boron and phosphorus, respectively.

Deposition and patterning of bias resistors

Typically, bias resistors are made of a doped polysilicon layer. The problem with polysilicon is that the type of the silicon changes during the lifetime of a Large Hadron Collider experiment. In our design, we use tungsten nitride (WN_x). WN_x is a practical material because it does not require a high temperature deposition process, works on both n- and p-type materials, can be easily patterned, and is fully compatible with the process chemicals. The deposition itself is done by sputtering. A mixture of nitrogen and argon is used as the sputtering gas, resulting in a uniform and reproducible layer. The thickness of the layer is approximately 60 nm and the

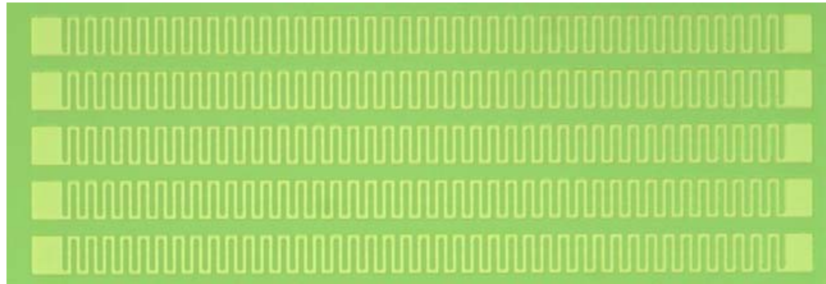

Figure 4.3: Finished bias resistors without contact metallizations.

target resistivity is about 1 MΩ. The bias resistors are patterned by lithography and etched with a combination of dry and wet etching. First, most of the layer is etched with RIE with CHF_3:O_2 chemistry and the etching is finished with hydrogen peroxide (H_2O_2) and de-ionized water (1:1), which leaves the underlying layers intact. Not all the chemistries used in our RIE are highly selective against silicon dioxide layers. A picture of finished bias resistors is shown in Figure 4.3. The width and the length of the bias resistors are 36 μm and 715 μm, respectively. A yield of more than 95% of working bias resistors is achieved with our process equipment. Later, during bonding, the faulty bias resistors are not connected to the read-out electronics.

Etching of contact openings

After the patterning of bias resistors, the process is continued with contact openings to substrate diffusions. The openings are relatively large and designed in such a way that they are not sensitive to over-etching. The openings are patterned with photolithography and etched with a buffered hydrogen fluoride (BHF) etch. Patterning is completed by resist removal.

Metallization

The metallization is done right after the resist removal. A 500-nm thick layer of aluminum is sputtered on the front side of the wafer and patterned by photolithography. The aluminum layer is etched with a solution containing phosphoric acid, currently Honeywell PS 80-16-4. After the patterning, the resist is once again removed. Figure 4.4 shows strip capacitor metallizations and metallizations connecting bias resistors to each substrate diffusion. Contact openings can be seen as three sharp "spots" in the metallization at the ends of the bias resistors.

Aluminum sintering

Aluminum sintering is done in a nitrogen (or forming gas) atmosphere. The purpose of this treatment is to improve the electrical contact between the aluminum and silicon.

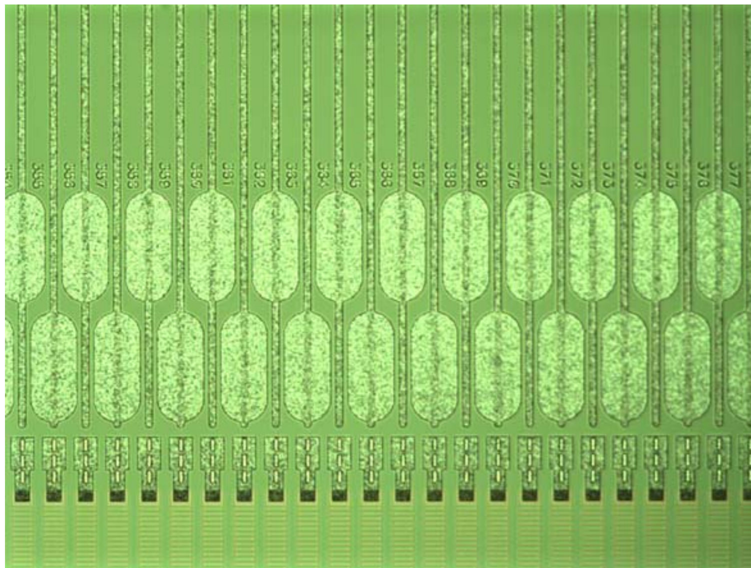

Figure 4.4: Close-up of bonding pads and the ends of bias resistors. The photograph was taken after metallization.

During sintering the grain size of the aluminum layer grows and the resistivity of the layer decreases. The time and temperature depends on the silicon material and possible thermal donor (TD) generation. Typical values for n-type MCz detectors are 30 min at 370°C, which does not generate TDs.

Passivation and passivation openings

The process is finished with a passivation layer. The purpose of this layer in our process is mostly to protect the detector surface from scratches and other external damage. We have used a plasma-enhanced chemical vapor deposition (PECVD) stack of silicon nitride and oxide.

The stack is patterned with photolithography and dry-etched with RIE. The etching process is quite relaxed since the aluminum layer allows us to over-etch for a sufficiently long time. Passivation deposition can be done either before or after aluminum sintering. The contact openings to the strip capacitors and bias line are large, facilitationg the easy probing and bonding of the samples. The contacts at the ends of the bias resistors are relatively small because of the limited space and the fact that they are only necessary during detector characterization (see Figure 4.1). Figure (4.5) shows finished strip detector and pad detector wafers ready for dicing and other back end processes.

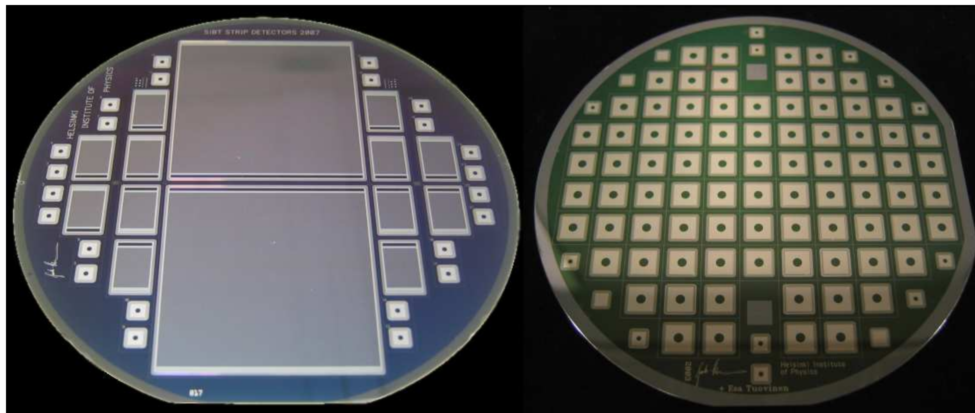

Figure 4.5: Finished strip and pad detector wafers.

4.3 Detector process on p-type wafers

The p-type process is quite similar to the n-type process. The implantations are reversed, e.g. boron on the back surface and phosphorus on the front surface, and both implantations are done after the first oxidation. The challenge in the p-type process is that there is a positive fixed charge in the oxide layer. This charge draws electrons to the silicon surface. Because of the low dopant concentration, these electrons can form an n-type channel, leading to increased surface currents. In order to alleviate this problem, additional implantation(s) are necessary. In our processes, patterned p-stop and/or p-spray field implantations have been used. More p-type process issues can be found in Publications 1, 4, and 5 of this thesis.

High resistivity p-type Czochralski silicon wafers can also be used instead of n-type wafers. In that case, the whole process is done as if the wafers were n-type, i.e. boron is implanted on the front surface and phosphorus on the back surface. During sintering, thermal donors are intentionally generated and the bulk is turned from dominantly boron-doped p-type silicon to thermal donor-doped n-type silicon. Such samples are characterized in Publication 5 of this thesis.

4.4 Thermal donor compensation

We have studied intentional thermal donor generation in order to probe its feasibility for tailoring initial full depletion voltages. The points of particular interest are the uniformity of the generated defects and the generation rate itself.

In our process, thermal donors were generated intentionally during aluminum sintering. The TD generation process is strongly dependent on temperature. Temperatures of 410°C, 430°C and 450°C were used in our studies. Figure 4.6 illustrates TD generation in silicon bulk at 430°C. The change in effective dopant concentration (generated TDs) was determined from the capacitance-voltage (CV) data. The sign

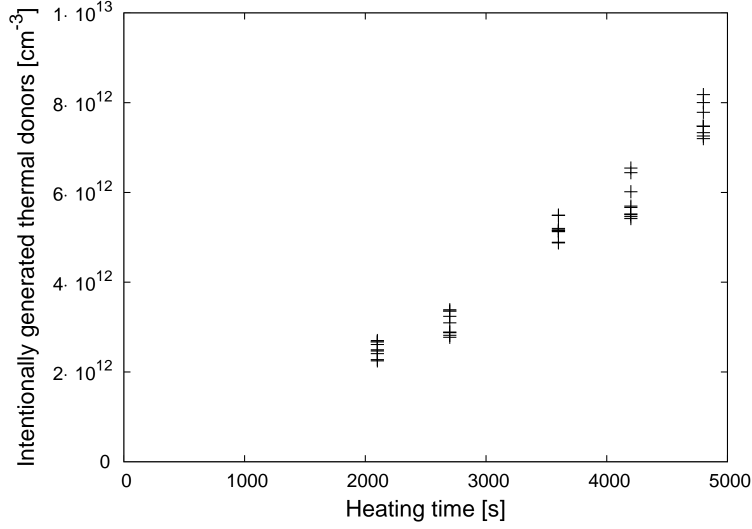

Figure 4.6: Thermal donor generation in silicon in extended annealing process at 430°C. Effective doping concentrations have been calculated from the capacitance-voltage data and the space charge sign is checked with the Transient Current Technique. The data are from Publication 1.

of space charge was checked with the Transient Current Technique (TCT). TCT and the CV method are described in detail in Section 5.5. TD generation was found to behave controllably and exhibited only minor radial deviations.

In Publication 1, these data were used to improve the model for thermal donor generation in high-resistivity silicon material. With the small modifications to the model proposed by Wada [16], the time- and temperature-dependent model for thermal donor generation can be expressed as:

$$N_{TD}(t,T) = a(1 - e^{-xt}) + N_{TD}(0,T) \qquad , \tag{4.1}$$

where t is time, T is the absolute temperature and, a is given by

$$a = c \times {O_i}^{\chi} \qquad , \tag{4.2}$$

where c is a fitting constant, O_i is the interstitial oxygen concentration, and χ is the reaction order. The x in Eq. 4.1 is given by

$$x = bO_iD_i \qquad , \tag{4.3}$$

where b is a fitting constant and D_i is the diffusion coefficient of the interstitial oxygen given by

$$D_i(T) = 0.13e^{-(E_A/kT)} \qquad (cm^2/s) \qquad , \tag{4.4}$$

where k is the Boltzmann constant and $E_A = 2.53eV$ is the activation energy of TD generation. After fitting the data to our model, the reaction order, χ, was found to be 1.89, which is close to the prediction of approximately 2 in Ref. [19].

It is well known that hydrogen can enhance the formation of the thermal donors in silicon [24] and can be seen e.g. after hydrogenation in PECVD plasma [25, 26]. PECVD process gases in general, contain hydrogen which is trapped in the growing layers. In our process, the hydrogen in the PECVD passivation layers had only a very small or negligible effect on the TD generation rate.

4.5 Process characterization

Our detector process was characterized with several measurement methods and supported by numerical simulations. Here I will present the results from process-related characterizations, including effective minority carrier lifetime measurements, ion implantation simulations, and bias resistor measurements. The characterization methods used in the radiation hardness studies will be described in the next chapter, even though i.e. leakage current measurements can also be used in process characterization.

Ion implantation characterization

Implantations are critical for the process. When working with high-resistivity substrates, one has to ensure that the masking layer blocks almost all of the ions. Figure 4.7 presents stopping simulation results for a 10 million-hit run for a 300-nm SiO_2 masking layer. The simulation was done with the SRIM 2008 software [27]. In the simulation, most of the ions were stopped at the depth of roughly at 250 nm. The tail of the distribution still spreads towards the edge of the simulation area and in fact one ion was transmitted into the lattice. With our implantation dose, one ion in ten million causes after oxidations final concentration of well under 10^{12} cm^{-3}. Thus it does not cause any problems.

Ion implantation profiles after high-temperature oxidation and annealing were simulated with the ICECREM software (see Figure 4.8). Deep profiles are wanted in our application, where the detectors have to stand voltages as high as 1000 V. Thus, smooth junctions are preferred. With our long oxidations, the junction depths are almost solely defined by the duration of the oxidation. Naturally, the implants also diffuse laterally, and with lateral diffusion of roughly 3.5 µm, implantation line widths will spread 7 µm. This was taken into account in mask design, where the minimum space between implant lines is 20 µm, thus leaving a large safety margin.

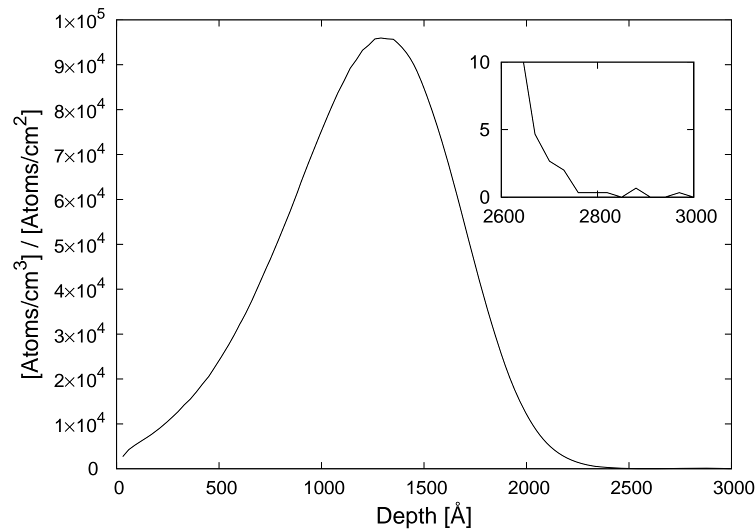

Figure 4.7: 30-keV boron stopping in 300-nm SiO_2 mask. Simulation of 10 million events with SRIM 2008 software [27].

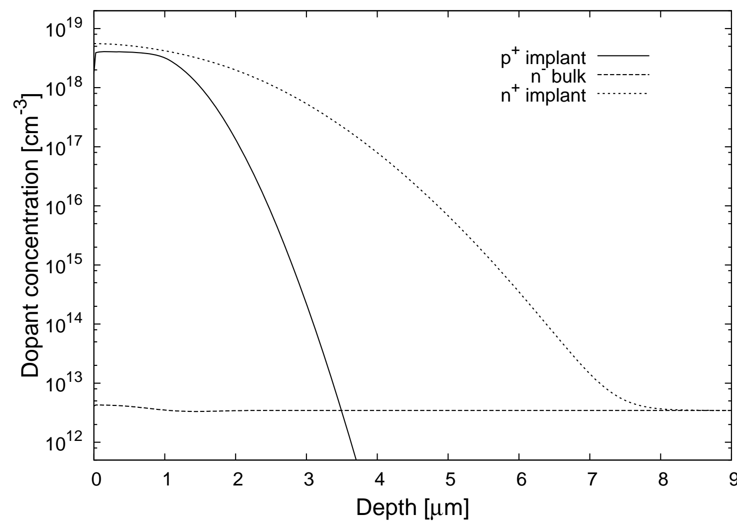

Figure 4.8: Implantation profiles in silicon.

Bias resistor values

The bias resistor values have a strong impact on the detector read-out. In order to map the performance of our tungsten nitride process, all the bias resistors were automatically probed from one full-size detector with 768 channels (see Figure 4.9). As can be seen from the picture, the distribution of resistance values is very uniform, with an average value of 955 kΩ and a standard deviation of 73 kΩ. The deviations from the trend are most probably due to minor masking faults (a small section of a

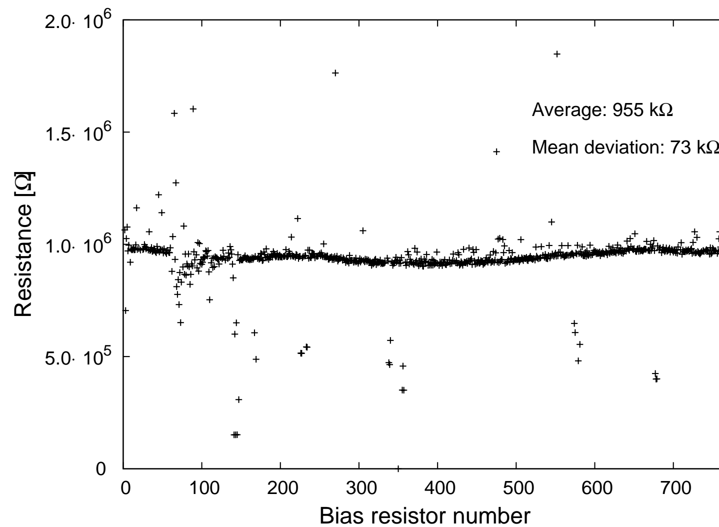

Figure 4.9: Bias resistor resistance values from one full-sized detector. Average and mean distribution values calculated from data after excluding bad data, e.g. no contact during measurement. Yield for the bias resistor process is greater than 95%.

bias resitor was shorted) or due to poor contacts during measurement. The contact pads at the ends of the bias resistors are relatively small, making automatic probing a little more challenging. The bias resistor measurement was done by our colleagues at the University of Karlsruhe, Germany.

Lifetime measurements

Minority carrier lifetimes were measured with the Microwave Detected Photoconductivity Decay method (μPCD) from monitor wafers. Despite the clean processing conditions, the possibility of metallic contamination is always present. These metallic impurities, i.e. iron and copper, shorten the minority carrier lifetime of the silicon bulk and increase the leakage current in processed components. Since the particle detectors are usually devices with a large active area, even a small localized contamination can increase the total leakage current of the detector significantly.

In the photoconductivity decay (PCD) method, the silicon sample is illuminated with a laser pulse. The recombination of the excess ehps, generated by the light, reduces the conductivity of the silicon. This decay in conductivity is measured by the reflectivity of the microwave signal, proportional to the conductivity of the sample. The measurement method is described in detail in Ref. [28]. The PCD method measures the so-called effective lifetime, which is a complex of the bulk and the surface lifetime. In order to suppress the surface effects, the sample is properly passivated (usually oxidized) and a corona charge is deposited on top of the sample.

The concentration of excess carriers generated by the laser decays exponentially

with the effective lifetime, τ_{eff} [28]:

$$\Delta n(t) = \Delta n(0) e^{-\frac{t}{\tau_{eff}}} \quad , \tag{4.5}$$

where $n(t)$ and $n(0)$ are the excess carrier concentrations, t is time, and τ_{eff} is given by:

$$\frac{1}{\tau_{eff}} = \frac{1}{\tau_B} + D\beta^2 \quad , \tag{4.6}$$

where τ_B is the bulk lifetime, D is the diffusion coefficient, and the parameter β is defined as:

$$\beta \tan(\frac{\beta T}{2}) = \frac{s_r}{D} \quad , \tag{4.7}$$

where T is the thickness of the sample and s_r is the surface recombination velocity.

The µPCD measurement unit uses a 902-nm wavelength pulsed laser for carrier generation, operating at cycles of 200 ns. During the measurement the laser power is kept constant. Prior to the measurement, the frequency of the microwave signal is adjusted to between 10 and 11 GHz in order to maximize the reflected signal. The measurement takes less than a second per data point, making it possible to map the whole wafer in a reasonable time. From these maps, we can monitor the cleanliness of our furnaces and other processes. Similar maps are also measured from some of the actual process wafers in order to validate the quality of the starting wafers. A set of lifetime maps can be seen in Figure 4.10. The horizontal lines in the map in Figure 4.10 a) are artefacts typical of high lifetime values. These lines are caused by the limited fitting time (20 ms) of the conductivity decay. The average lifetime in this wafer was very high, 9 ms. The wafer in the map in Figure 4.10 b) was from a contaminated box of wafers. The average lifetime in this contaminated wafer was only 300 µs. The whole box of wafers was discarded after further inspection. Other than occasional tweezer marks (Figure 4.10 c)), one can see marks coming from the quartz boat used during the oxidations. In general, lifetime values greater than 5 ms are excellent, values between 1-5 ms are adequate and less than 1 ms are bad.

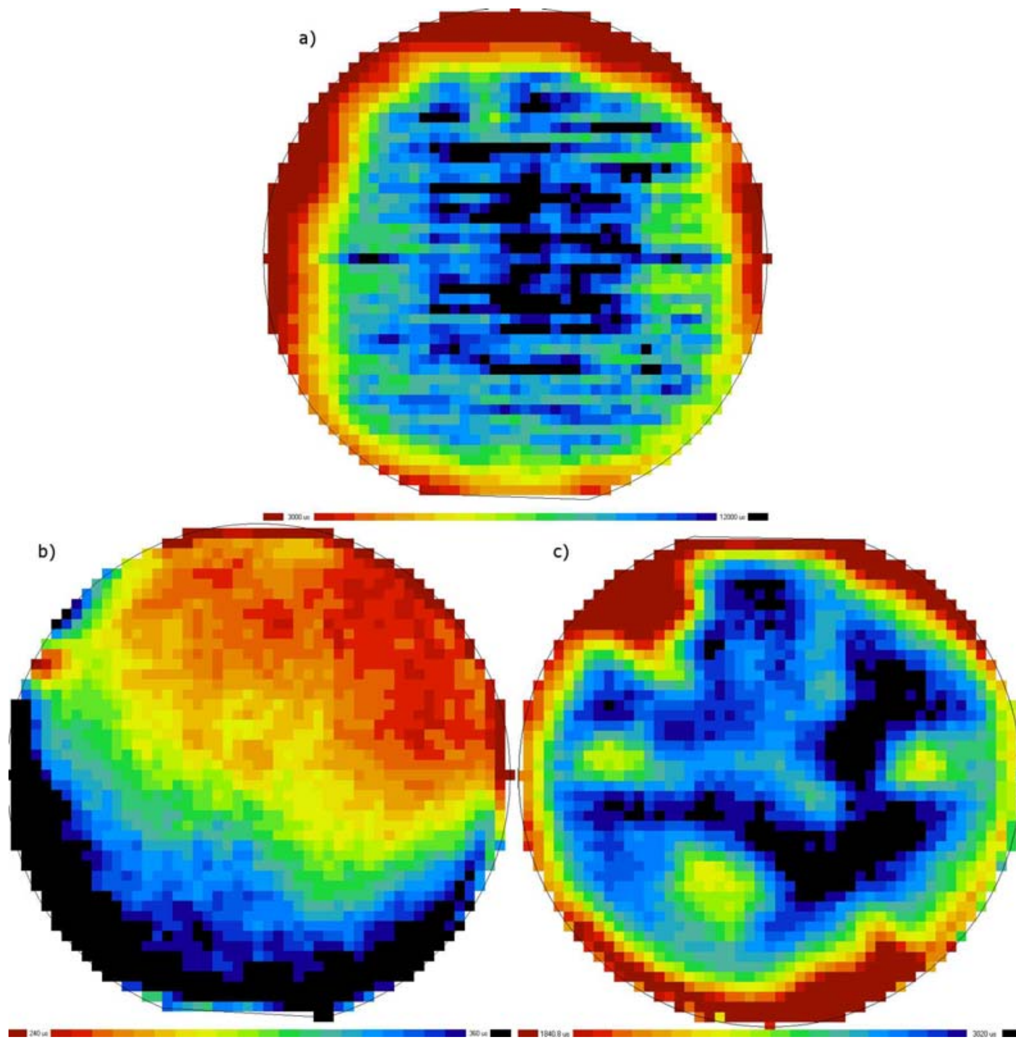

Figure 4.10: The Good, the Bad, and the Ugly of lifetime maps. a) Excellent lifetime values (3 ms to 12 ms, average 8.2 ms) b) Contaminated wafer (240 µs to 360 µs) and c) tweezer mark in the upper left edge of the wafer and possibly contamination from the quartz boat in the lower part of the map.

Chapter 5

Radiation hardness of silicon detectors

As the expected fluences in high-energy physics experiments increase, the radiation hardness of the detectors becomes more and more important. Radiation damage causes increasing detector leakage currents, changes in the effective doping concentration, and, ultimately, after heavy fluencies, significant deterioration of charge collection efficiency (CCE) as a result of trapping. Radiation hardness is the ability of the detector to resist these changes. Radiation hardness alone does not make a detector good particle detector. A good initial performance is also required.

Radiation hardness has been studied extensively for several years in several instances, i.e. the CERN RD48 collaboration [9] and nowadays the CERN RD50 collaboration [3].

5.1 NIEL scaling hypothesis

The non-ionizing energy loss (NIEL) is the fraction of the energy that the incident particle transfers to the silicon lattice via elastic scattering. This energy is responsible for the displacement of the atoms in the material. The deteorioration is dependent on the energy, the type, and the fluence of the particles. The resulting damage can be scaled with NIEL values. The NIEL values for various particles over large energy ranges can be found in Ref. [29].

The basic assumption in NIEL scaling is that any change in the material resulting from displacement damage scales linearly with the amount of energy imparted in the collision. The NIEL values can be expressed through the displacement damage cross-section, D. The D values are given in MeVmb and the NIEL-values are expressed in keVcm^2/g; for silicon 100 MeVmb $=$ 2.144 keVcm^2/g. According to the ASTM standard, the displacement damage cross-section for 1 MeV neutrons is set as a

normalizing value: $D_n(E = 1MeV) = 95MeVmb$ [30]. The damage efficiency of a given particle can be expressed through the hardness factor, κ:

$$\kappa_{particle}(E) = \frac{D_{particle}(E)}{D_n(E = 1MeV)} \quad , \tag{5.1}$$

where $D_{particle}$ is the displacement damage cross-section for the particle.

In radiation hardness studies the results are often scaled to 1 MeV neutron equivalent values with the help of the hardness factors. The NIEL scaling should be used with caution. There is no real understanding of why the scaling should work and there is even evidence of significant violations [1, 31]. Therefore it can only be used to cancel out most of the particle type and energy dependencies from the experimental data.

5.2 Radiation effects in silicon detectors

The radiation effects in silicon can be split into two basic mechanisms, namely bulk and surface damage. Bulk damage is caused by the displacement of atoms from their lattice sites and surface damage is caused by passivation layer degradation resulting from the build-up of a charge in the layers. The amount and nature of the damage are strongly dependent on the energy and the type of the particle traversing through the detector. Figure 5.1 presents simulated damage distributions for different particles. As a rule of thumb, charged and low-energy particles cause more point-like damage and neutral particles cause cluster-like damage in the silicon lattice [31]. The nature of these clusters is not well known; one proposed model for the clusters consists of a sphere with a core (Region 1) and an outer sphere (Region 2). Divacancies exist in both regions, but di-interstitial-related defects are only located in the Region 2 because of the greater mobility of the interstitials [32]. The charge exchange between these regions is used to explain macroscopic phenomena.

Surface damage

Ionizing radiation causes degradation in surface passivation layers. Ionizing particles induce holes in the layer. A part of this charge is trapped in the layer and a part will interact with the silicon-oxide interface, increasing the interface state density [33]. These changes can cause e.g. increased signal sharing between neighboring strips. The device structure and the choice of the process parameters have a strong influence on how severe this issue is. With proper process optimization these issues can be minimized [12]. In our process this means e.g. use of dry oxidation in the strip capacitor insulation layer (best quality) and the use of <100> wafers (lower interstate trap density).

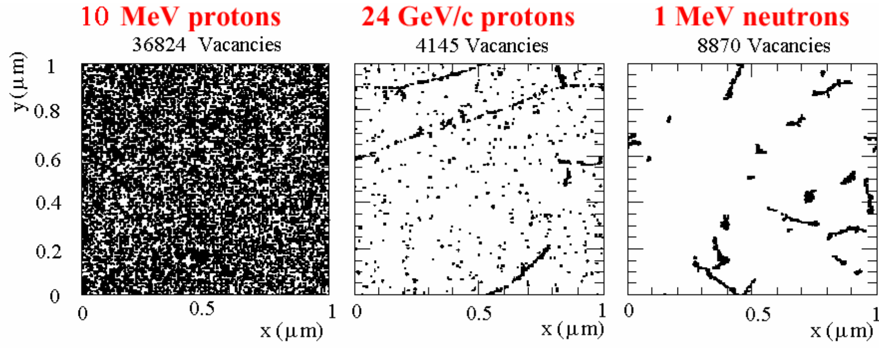

Figure 5.1: The initial distribution of vacancies produced by different kinds of radiation. The plots are projections over 1 μm of depth and all the fluencies correspond to 10^{14} cm^{-2} [31].

Bulk damage

Bulk damage is caused by the incident radiation displacing atoms from their lattice sites. This process generates vacancy interstitial pairs, Frenkel pairs [1]. If enough energy is transferred in the initial collision, the so-called primary-knock-on-atom gets enough energy to create a new Frenkel pair. These damage cascades give rise to the formation of damage clusters. Most of the pairs recombine with each other, but some of the defects diffuse apart. Both vacancies and interstitial silicon atoms are mobile at room temperature. Vacancies and interstitials can in turn combine with other defects and impurities, creating more complex defects, e.g. divacancies (V_2), vacancy-oxygen pairs (V-O), divacancy-oxygen complexes (V_2O) etc. More complex defects are usually less mobile and i.e. divacancy-type defects are more harmful to the detectors.

The defect complexes create electrical states in the silicon band gap. Depending on the position of these levels, they can have a three-fold effect on the electrical properties of the silicon.

Leakage current

An increase in the deep energy levels near the middle of the band gap causes an increase in the leakage current. These energy levels act as generation and recombination centers. It has been found experimentally that the leakage current increases linearly with fluence [1] and can be expressed through a proportionality constant, α, called the current-related damage rate:

$$\alpha = \frac{I}{vol \times \Phi_{eq}} \quad , \tag{5.2}$$

where vol is the active volume of the detector and Φ_{eq} is the 1 MeV equivalent fluence. The leakage current is exponentially dependent on the temperature and the

values have to be normalized before analysis. α has been measured to be material-independent [34] and has a value of α(4min/80°C) $=$ 4.56 $\times$ 10^{-17} A/cm after beneficial annealing [35]. The issue can be alleviated with proper cooling of the detectors, because of the strong dependence on the temperature. Modern high-energy physics experiments require a lot of read-out electronics. Electronics dissipate a lot of heat and require cooling. The same cooling can be used to cool down the silicon detectors. Large experiments are typically performed at reduced temperatures of -10°C to -20°C. For detector characterization, large leakage currents pose a challenge and heavily irradiated detectors have to be measured at reduced temperatures.

Evolution of effective doping concentration

The removal of existing dopants from their active sites and the creation of new charged defect states near the band edges changes the effective doping concentration. In n-type silicon, the removal of phosphorus atoms and generation of new acceptor states leads initially to a reduction in the effective dopant concentration and the detector will eventually go through space charge sign inversion (SCSI). After SCSI the effective doping concentration will increase monotonically. As a result, the depletion voltage needed will increase and finally reach the breakdown voltage or be too much for the power supply. This will lead to a significant loss of charge because of the fact that only a part of the silicon bulk can be depleted. Figure 5.2 presents the typical effective doping concentration behavior measured from our n-type float-zone silicon detectors. The slope of the effective dopant concentration after the minimum, the β-parameter, in Publication 2 was found to be 0.0058, i.e. 35% higher than for the Cz-Si used in the same study. Even higher discrepancies have been reported in Ref. [1]. In p-type silicon, acceptor states dominate the effective doping concentration the whole time. There is usually an initial dip in the effective doping concentration prior to the normal steady increase.

Charge carrier trapping

The third process-degrading behavior of the detectors is trapping. Some of the charge carriers are captured by the trap levels and are not released in time since the detrapping time is too long compared to the typical shaping time of the read-out electronics. At first, trapping is not critical, as just a small fraction of the generated signal charge is lost. After heavy irradiation (1 MeV equiv. fluence of 10^{15} cm^{-2}), the concentration of traps is so large that even if the detector could be fully depleted, most of the charge is lost as a result of the trapping. Combined with the increased leakage current, this will be devastating to the signal-to-noise ratio (SNR) and ultimately, the signal cannot be distinguished from the noise.

To make the picture even more complicated, detrapping, the counter-process for trapping, is exponentially dependent on temperature. This opens up possibilities for the cryogenic operation of detectors. At low temperatures, filled trap states stay

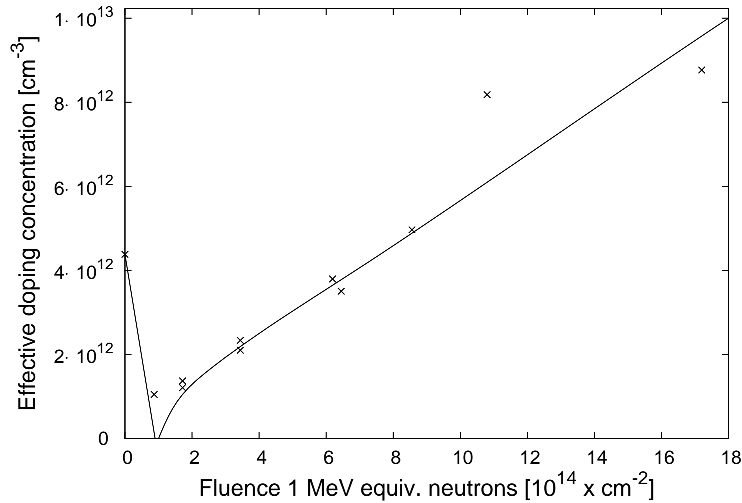

Figure 5.2: Evolution of effective doping concentration in n-type silicon after 10 MeV proton irradiation. The data are from Publication 2.

filled for the duration of the measurement. This can be used to significantly reduce trapping and thus improve charge collection efficiency.

The effective trapping probability does not scale with NIEL when comparing neutrons with charged hadrons [36]. The effective trapping probabilities after charged hadron irradiations are 30-40% larger than after neutron irradiations.

Annealing of the radiation damage

It is well known that the defects go through changes during long-term storage at room temperature [1]. Vacancies and interstitials in silicon are unstable. They migrate through the bulk and in the process, they recombine, annihilate, and react with other defects, forming new defects. Certain impurities can also capture vacancies and interstitials and form stable complexes in the process.

It is proposed that radiation produces an equal amount of vacancies and interstitials and that the concentration of radiation-induced defects is higher than the concentration of self-interstitials. Many of the vacancies and interstitials are annihilated right after production. Interstitials are more mobile than vacancies and the concentration of interstitials decays more rapidly than the concentration of vacancies. It is proposed [37] that vacancy-interstitial annihilation and interstitial migration to the sinks, oxygen for vacancies and carbon for interstitials, take place during the first 0.2 seconds, vacancy-phosphorus complex formation and decomposition during the period $10^3 - 10^4$ seconds and di-vacancy-related annealing during the period $10^7 - 10^8$ seconds. These processes are also called short-term beneficial annealing, the stable damage part, and reverse annealing [1].

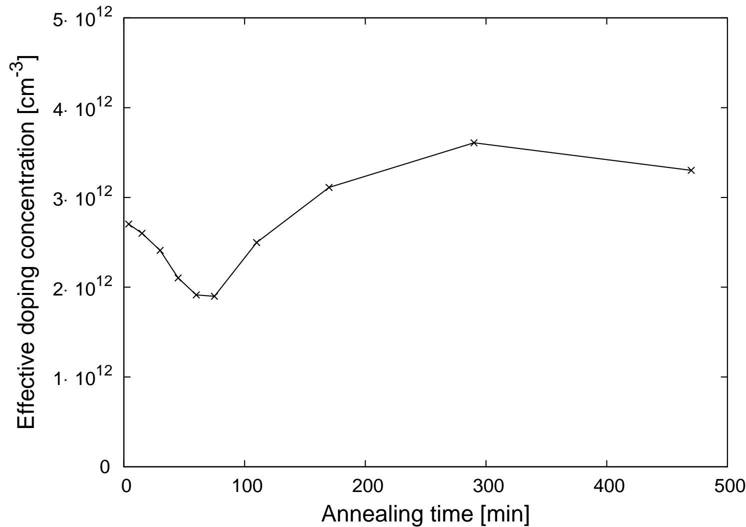

Figure 5.3: Typical evolution of effective doping concentration as a function of annealing time. The annealing was performed at 80°C. The magnetic Czochralski silicon pad detector was irradiated to 1.6 $\times 10^{14}$ 1 MeV neutron equivalent fluence by 20 MeV protons [38].

The time constants for these processes have been found to be independent of the fluence [1]. Since the time constants are relatively large, the annealing studies are usually carried out at elevated temperatures, typically 80°C. If a comparison with room temperature annealing is required, acceleration factors can be used to convert elevated temperature time scales to a room temperature time scale [1]. Inversely, operating detectors at the reduced temperatures has effects on the annealing.

In the detectors, the annealing processes have effects on many of the important parameters. The leakage current decreases monotonically with the annealing time. On the other hand, the effective doping concentration decreases during beneficial annealing until it reaches a minimum. After this point, the effective doping concentration starts to increase (reverse annealing). Typical effective doping concentration behavior measured from our n-type detector is illustrated in Figure 5.3.

There are only a few studies on the annealing of traps. The annealing properties of effective trapping probabilities are characterized in Reference [36]. The effective trapping probabilities for electrons and holes were found to decrease by 30% and increase by 35%, respectively, after annealing. The time scale for this process was approximately 100 hours (10^5 s) at 60°C. The annealing of trapping probabilities is a slow process compared to the annealing of other types of radiation damage.

5.3 Effect of oxygen on radiation hardness

The beneficial effect of oxygen on radiation hardness was first found while studying Czochralski silicon (Cz-Si) [1]. At the same time, the effect of carbon on radiation hardness was also studied. Unfortunately, in the 1990s, there was no high-resistivity Cz-Si available. In an oxygen-enriched material, the effective doping concentration changed less when it was irradiated with charged hadrons. It was found that the oxygen in silicon captures vacancies, forming vacancy-oxygen complexes. This process happens at the expense of the formation of di-vacancy (V_2) complexes, di-vacancy oxygen (V_2O) complexes, etc. As a rule of thumb, the more vacancies a complex has, the more harmful it is. Oxygen makes complexes less harmful, too. In fact, the V-O complex is relatively harmless with energy levels relatively distant from the mid-gap. Carbon was found to be detrimental to radiation hardness. This was probably due to the chain reaction: interstitial carbon reacted more with silicon interstitials, causing a decrease in vacancy-interstitial annihilation and consequently an increase in V_2 formation.

Unfortunately, oxygen does not affect increasing detector leakage current and trapping. Additionally, the beneficial effect of oxygen is not evident when the material is irradiated with neutrons [1]. This is probably due to the cluster-like damage formation. The concentration of vacancies inside clusters is so huge that the higher oxygen concentration cannot effectively prevent the formation of more harmful defect complexes.

After the discovery of the beneficial effect of oxygen, studies concentrated on so-called diffusion oxygenated float-zone silicon (DOFZ) [1]. DOFZ is made from a high-purity float-zone silicon by annealing oxidized wafers at a high temperature (> 1000°C) for several hours. As a result, some of the oxygen from the silicon dioxide layer diffuses into the silicon lattice. This process results in an interstitial oxygen concentration of approximately 10^{17} cm^{-3}.

Since the emergence of high-resistivity magnetic Czochralski silicon (MCz-Si) in 2002, interest has boomed. Our group was the first to demonstrate the potential use of MCz-Si in particle detector fabrication [21]. Czochralski silicon has an intrinsically high concentration of interstitial oxygen and was found to show potentially good radiation hardness properties. Lately, the research in the framework of CERN RD50 (the successor to RD48) has concentrated more and more on MCz-Si.

Not all the effects of oxygen have yet been found. In was found in our paper with Zheng Li et al. [39] that gamma irradiation generates a net positive space charge in materials with a high oxygen content, namely MCz-Si, whereas in regular FZ-Si the net space charge is negative. Furthermore it was found in Ref. [40] that with gamma irradiation it was possible to cause space charge sign re-inversion in previously neutron-irradiated samples. The generation of a negative or positive space charge has a clear dependence on the oxygen concentration. It has been thought that the effect is connected with the activation or reactivation of thermal donors in silicon.

It is quite obvious that the picture will be even more complicated if more types of irradiation are combined.

5.4 Advantages of p-type detectors

P-type detectors have some inherent advantages over n-type detectors and therefore there has been growing interest in studying p-type silicon. There is no space charge sign inversion (SCSI) in p-type material. This ensures that the electric field remains on the segmented side, which also results in higher charge collection efficiency (CCE) [41]. Electrons are collected from the segmented side. Electrons have higher mobility than holes, leading to higher CCE in heavily irradiated detectors. In other words, under heavy trapping, the charge is collected from a greater distance than in the case of hole collection. Recent studies have also indicated that electrons have longer effective trapping times, i.e. an average electron travels for a longer time (and distance) in silicon than holes [36]. These phenomena are true for both MCz-Si and FZ-Si.

The price one has to pay for these benefits is the more complicated process (see Section 4.3). One or two additional implantations are needed in order to suppress unwanted surface currents in p-type silicon. Furthermore, an additional mask level is required if p-stop implantation is wanted. A simpler field implantation (p-spray) does not require an extra mask level.

In p-type MCz-Si, it is possible to introduce thermal donors into the material. These TDs can be used to tailor the full depletion voltage of the detectors. TDs compensate some of the initial acceptors, leading to lower initial operating voltages. Furthermore, TDs seem to be very tolerant to radiation and do not exhibit the same kind of donor removal as phosphorus does, as described in Publication 5 of this thesis.

5.5 Characterization of detectors

Thorough characterization of detectors was performed prior to and after irradiations. Typical parameters used for definition prior to irradiation include full depletion voltage, V_{fd}, and leakage current at full depletion. After irradiation, typical parameters include V_{fd} evolution, charge collection efficiency, CCE, leakage current at full depletion, and several other types of parameters derived from previous data, including deviations from the hardness factor, κ, the increase in the leakage current vs. fluence, α, and the introduction rate of negative space charge beyond inversion, β-parameter, to name a few. Typically, many of these parameters can be defined with many different methods and many of the methods are very time-consuming.

Figure 5.4: Small test diode placed in the probe station at CERN SSD laboratory.

Current-Voltage and Capacitance-Voltage measurements

Current-Voltage (IV) and Capacitance-Voltage (CV) measurements are important basic characterization measurements. The measurements were performed in a probe station protected from the light. The setup consists of a computer-controlled source meter unit (SMU), a current meter, and a capacitance meter. The sample is placed on a vacuum chuck and the contact at the back surface is provided through the chuck. The ambient temperature is recorded for correction purposes, particularly of IV measurement data. The front contacts are provided through probe needles (see Figure 5.4). To perform IV or CV measurement usually take 5 to 10 minutes.

The IV measurement is usually done using both the SMU and the current meter. A high voltage is applied to the back contact with the SMU, simultaneously measuring the total current. The current meter is used to measure the active area current, the total current minus the guard ring current. From the IV data, we can extract the value for the leakage current at full depletion and the general behavior of the current during biasing. The leakage current is strongly dependent on the temperature and thus it is important to monitor the ambient temperature during the measurement.

CV measurement is an easy way to probe the full-depletion voltage of the detectors. CV measurement is usually done at room temperature with a 10kHz measurement frequency. High leakage currents can interfere with the measurement e.g. heavily irradiated detectors require cooling during measurements. CV data are usually plotted in a double logarithmic graph. As the applied voltage increases, the depletion region extends towards the other contact, reducing the measured capacitance. When the depletion region reaches the other contact, the capacitance value saturates. Lines

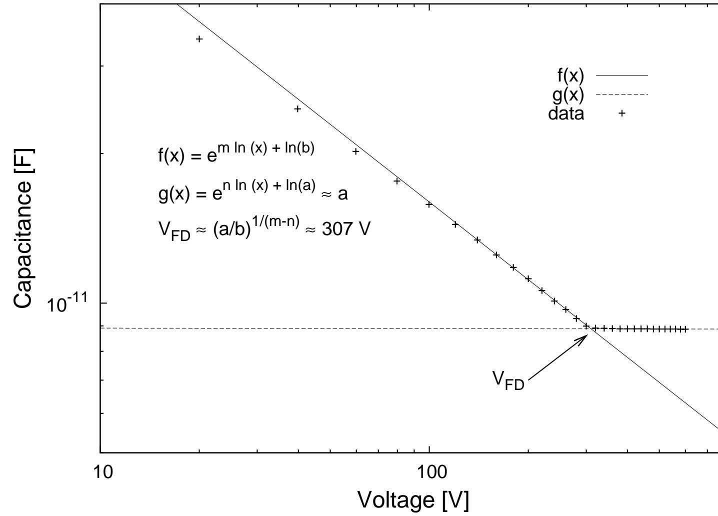

Figure 5.5: Logarithmic CV graphs and the method for defining V_{fd}. The diode is under-depleted before V_{fd} and saturates right after depletion.

are fitted to the data points before and after saturation and the V_{fd} is extracted from the intersection of the lines. See Figure 5.5 for an example of CV data. Typically, the fitting is more challenging for heavily irradiated detectors, i.e. the beginning of saturation is not so evident.

Transient current technique (TCT)

The Transient Current Technique method was developed in the 1990's by the Ioffe Institute (St. Petersburg, Russia) and Brookhaven National Lab (USA) [42]. With TCT, it is possible to determine several device parameters, including the full depletion voltage, V_{fd}, the sign of the space charge in the device bulk, and effective trapping time [43, 44]. In TCT measurement, the sample is illuminated with a laser that creates electron hole pairs within a few micrometers of the surface. The charge carriers are separated in the electric field and the ones drifting through the whole detector bulk are measured. Whether we measure the electron or hole current depends on which contact is illuminated (see Figure 5.6).

If the p^+ contact of the device is illuminated, the current gathered is coming from electrons. Similarly, if the n^+ contact is illuminated, the hole current is monitored. The current coming from the other type of charge carrier is collected very fast and the signal is damped by the limited rise-time of the data acquisition electronics. The basic mechanism used in TCT measurement is illustrated in Figure 5.7.

Depending on the conducting type of the device bulk, the electric field, i.e. the collecting junction, is either on the front or back of the detector. If measured illuminating the front while the collecting junction is on the same side, a descending

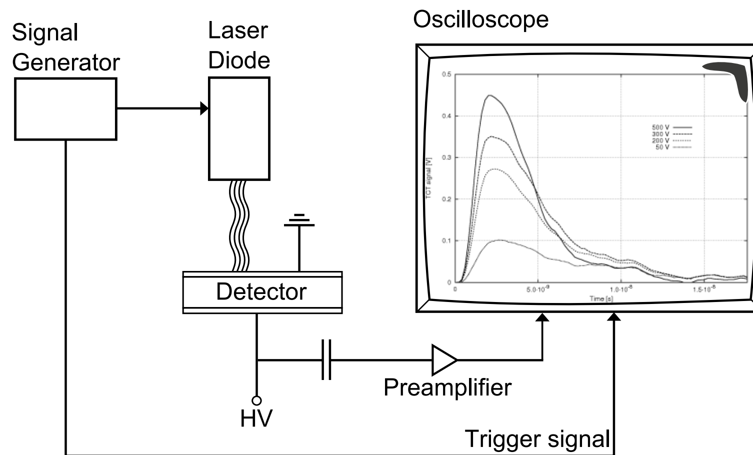

Figure 5.6: Schematic layout of a TCT measurement setup.

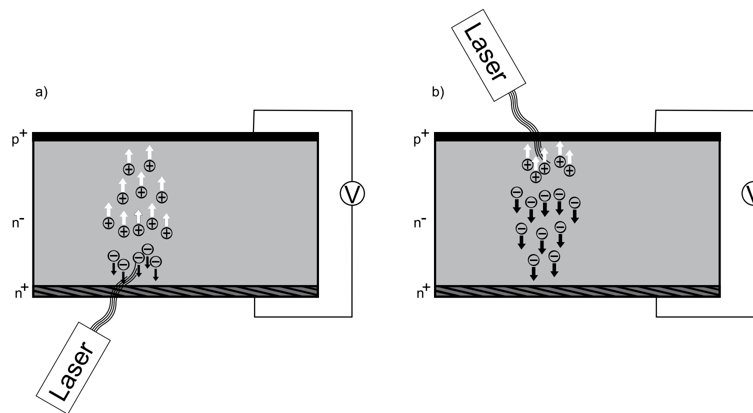

Figure 5.7: Transient current technique: a) hole-dominated current when the n^+ contact is illuminated, and b) electron-dominated signal when the p^+ contact is illuminated.

electron transient signal is measured. If the collecting junction is on the back junction an ascending signal is measured. Similarly, if measured illuminating the back side, an ascending/descending signal is measured if the collecting signal is on the front/back, respectively.

When measuring heavily irradiated samples, trapping cannot be neglected. The trapping time becomes comparable to the drift time in silicon bulk and thus affects the pulse shape. The data have to be corrected before any conclusions can be drawn on the shape of the curve.

Figure 5.8 shows an electron signal measured from an n-type sample. First, we can see that the electron signal is collected within approximately 10 ns. The type of the bulk can be seen from the shape of the curves. The signal is descending after an initial rise, e.g. the electrons are moving from high-field to low-field. Thus the

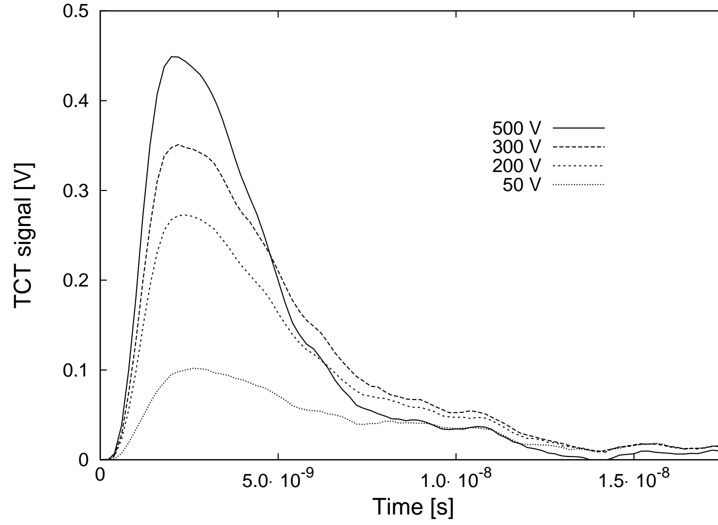

Figure 5.8: Current transients of an electron-dominated signal.

junction is still on the front of the detector and the bulk is n-type. Full depletion can be probed more accurately when measuring from the low-field side of the detector. Hardly any charge is collected before depletion and a large increase in the measured signal occurs after depletion. Trapping times require more complex calculations.

Charge collection efficiency

Charge collection efficiency measurements (CCE) or charge-voltage measurements are important detector characterization methods. They directly probe the collected charge and thus the performance of the detector. The charge can be generated with many methods e.g. an IR laser, beta source etc. It is critical for the correct interpretation of the results that the charge generation with the source is stable in time. The CCE defined by the collected charge, Q_{coll}, divided by the collected charge measured from an unirradiated reference detector, Q_{ref}.

$$CCE = \frac{Q_{coll}}{Q_{ref}} \tag{5.3}$$

In a real irradiated detector, the charge collection efficiency can be split into two terms, the geometrical and trapping terms. The geometrical term, CCE_{geom}, takes into account the possible under-depletion resulting from insufficient biasing and the trapping term, CCE_{trap}, takes into account the exponential relation to the trapping time, τ_{trap}. The determination of the charge collection efficiency (CCE) is based on the formula:

$$CCE = CCE_{geom} \times CCE_{trap} = w/d \times e^{\frac{t}{\tau_{trap}}} \quad , \tag{5.4}$$

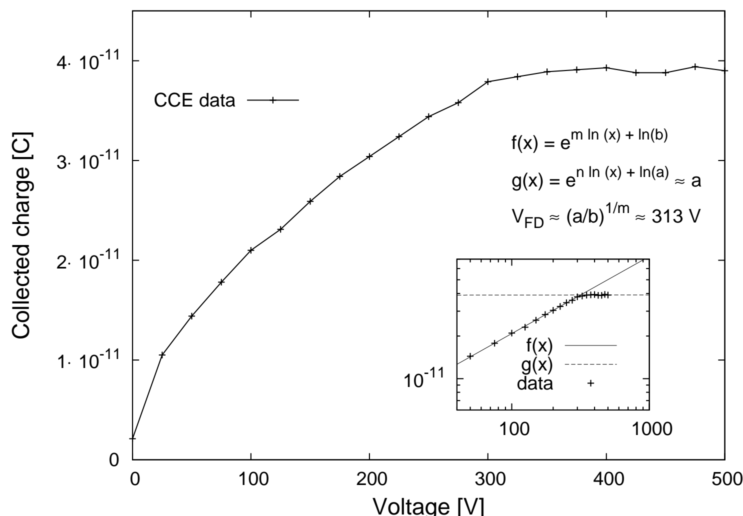

Figure 5.9: Experimental data from a QV measurement. The V_{fd} value has also been extracted from the data.

where w is the width of the space charge region in the device bulk and d is the thickness of the device. CCE does not show how much charge one can collect from, it just shows how well the detector being tested retains the ability to collect a charge.

The data from a Charge-Voltage measurement are presented in Figure 5.9. The measurement was performed with the TCT setup. The charge created in the sample with the laser pulse corresponds roughly to the charge deposited by 10,000 minimum ionizing particles. Again the collected charge increases as the depletion region extends towards the other contact. After full depletion, the collected charge saturates. In the insert in Figure 5.9, the full-depletion voltage is extracted from the data in the same way as from the CV data.

Trapping affects the charge collection efficiency significantly. Charge collection versus fluence for wafers of different thickness was simulated in order to explain important features affecting charge collection. The simulation takes into account linear trapping, but does not include the weighting field effect. Several important features can be seen from Figure 5.10. First, the maximum collected charge depends linearly on the thickness of the wafer. Second, with thicker detectors the signal starts to fall drastically when the bulk is not fully depleted any more. The bias voltage was set to 500 volts in the simulation. Still, the collected charge stays greater in the thick detectors after the detector is not fully depleted any more. Third, trapping affects all the samples sooner or later, i.e. for the 300-µm simulation, some 25% of the deposited charge is lost as a result of trapping at a 1 MeV equivalent fluence of 10^{15}. The β-parameter in the picture is the introduction rate of the negative space charge for standard float-zone samples taken from Ref. [1]. According to our results in Publication 2, the β-parameter for Czochralski silicon irradiated with

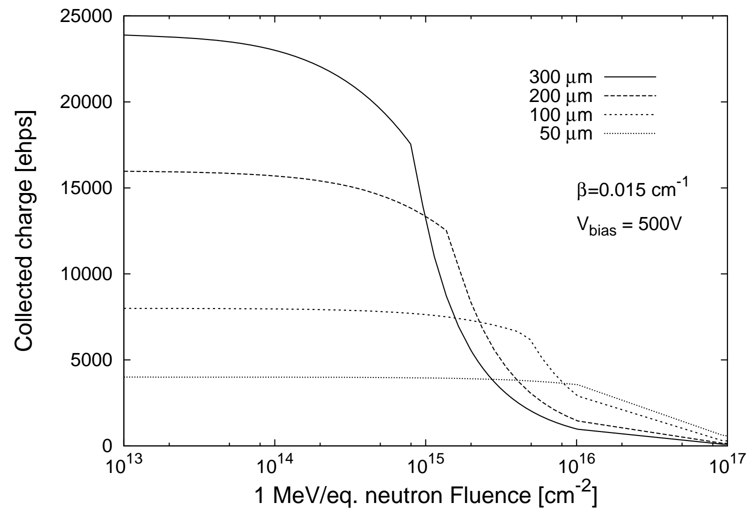

Figure 5.10: Collected charge vs. fluence simulation. Wafer thickness is varied in different data sets.

charged particles is approximately 0.005. In this simulation, it would mean that the under-biasing would occur after higher fluence, roughly 2.5×10^{15}. In that case the effect of trapping would be even more evident, as more than 50% of the charge deposited in a 300-μm detector would be lost at the neutron equivalent fluence of 2.5×10^{15}.

Chapter 6

Conclusions

In this work, we have processed detectors on both n- and p-type silicon and characterized both wafer types as particle detector substrates. It was shown that with our process it is possible to produce excellent pad and strip detectors for research applications. The Micro- and Nanofabrication Center has all the essential process equipment in-house. From the scientific point of view, the possibility of having access and being able to control all the process parameters adds depth to the interpretation of the results. It was shown that the electrical properties of the detectors processed on these high-resistivity Czochralski wafers, i.e. full depletion voltage and leakage current, are comparable to those of traditional high-purity float-zone silicon detectors. In general, there is no huge difference between processing MCz-Si and Fz-Si. Because of thermal donor generation, one has to avoid or be careful with temperatures between 400°C and 700°C when processing MCz-Si.

Lifetime measurements after oxidation processes indicate that both p- and n-type, float-zone and magnetic Czochralski wafers have sufficiently long lifetimes, i.e. more than 2 ms. Moreover, the lifetime maps reveal a normal circular symmetry with lower lifetime values at the edges [21]. Lifetime characterization results were presented in detail in Publication 5. At the center of the wafer the lifetime was as high as 10 ms and the average lifetime was even as high as 8.2 ms in n-type magnetic Czochralski silicon. These values can be considered excellent by all standards.

Effort was put into implementing thermal donors into our process and characterizing their generation inside the detector wafers. The thermal donors were found to be a practical way to tailor effective dopant concentration, especially in p-type magnetic Czochralski silicon, making it possible to process easily and cost-effectively detectors that deplete with less than 100 volts. Thermal donor generation was found to be a uniform and well-controllable process. Our improved model for thermal donor generation in this material, presented in Publication 1, can be used to accurately predict the final concentrations of thermal donors. In Publication 5, thermal donor generation

was found to be insensitive to the incorporation of hydrogen into the silicon during the normal process steps.

In irradiation studies diodes made on Czochralski silicon and float-zone silicon control samples were irradiated up to the fluences of 10^{15} 1 MeV equivalent neutrons/cm^2. As expected, magnetic Czochralski silicon showed good radiation hardness properties when compared with regular float-zone silicon detectors. The possible space charge sign inversion in n-type silicon was confirmed by the transient current technique (TCT). Compared to phosphorus-doped n-type detectors, detectors with thermal donor-induced space charge sign inversion were found to be especially tolerant to high-energy protons (Publication 5).

In the future, our research will concentrate more on real segmented detectors. In the past, the research has been concentrated on studying the leakage current and evolution of full depletion voltage properties. However as the fluencies in high-energy physics experiments increase, the degradation of the collected charge or charge collection efficiency are becoming more and more critical for detector operation. We will be concentrating more on characterizing charge collection in detector structures. We will also continue studying other alternative methods to achieve radiation tolerance in extreme environments, e.g. forward-biased operation in "cryogenic" conditions (-50°C and below).

Bibliography

[1] G. Lindström et al. Radiation hard silicon detectors – developments by the RD48 (ROSE) collaboration. *Nucl. Instrum. Methods Phys. Res., Sect. A*, 466:308–326, 2001.

[2] M. Moll et al. Development of radiation hard sensors for very high luminosity colliders – CERN-RD50 project. *Nucl. Instrum. Methods Phys. Res., Sect. A*, 511:97–105, 2003.

[3] CERN RD50 Research programme, `http://rd50.web.cern.ch/RD50/`.

[4] J. Härkönen et al. (incl. E. Tuovinen). Recent results from the CERN RD39 collaboration on super-radiation hard cryogenic silicon detectors for LHC and LHC upgrade. *Nucl. Instrum. Methods Phys. Res., Sect. A*, 535:384–388, 2004.

[5] V. Eremin et al. Current injected detectors at super-LHC program. *Nucl. Instrum. Methods Phys. Res., Sect. A*, 583:91–98, 2007.

[6] P. Luukka et al. The operation and performance of current injected detector (CID). *Nucl. Instrum. Methods Phys. Res., Sect. A*, 581:356–360, 2007.

[7] W. Zulehner. The growth of highly pure silicon crystals. *Metrologia*, 31:255–261, 1994.

[8] G. Lutz. *Semiconductor radiation detectors: Device physics*. Springer-Verlag, 2001.

[9] CERN RD48 Research programme, `http://rd48.web.cern.ch/RD48/`.

[10] W. Zulehner. Czochralski growth of silicon. *J. Cryst. Growth*, 65:189–213, 1983.

[11] S.M. Sze. *Physics of semiconductor devices*. John Wiley & Sons, 2nd edition, 1981.

[12] W-M Yao. Review of particle physics. *J. Phys. G: Nucl. Part. Phys.*, 33:1, 2006.

[13] W. Zulehner. Historical overview of silicon crystal development. *Mater. Sci. Eng. B*, 73:7–15, 2000.

[14] V. Savolainen et al. Simulation of large-scale silicon melt flow in magnetic Czochralski growth. *J. Cryst. Growth*, 243(2):243–260, 2002.

[15] G.S. Oerhlein. Silicon–oxygen complexes containing three oxygen atoms as the dominant thermal donor species in heat-treated oxygen-containing silicon. *J. Appl. Phys.*, 54:5453–5455, 1983.

[16] K. Wada. United model for formation kinetics of oxygen thermal donors in silicon. *Phys. Rev. B*, 30:5884–5895, 1984.

[17] A. Ourmazd et al. Oxygen-related thermal donors in silicon: A new structural and kinetic model. *J. Appl. Phys.*, 56:1670–1681, 1984.

[18] R. Jones, editor. *Early Stages of Oxygen Precipitation in Silicon*. Kluwer Academic, 1996.

[19] Joo Lee Young, J. von Boehm, and R. M. Nieminen. Simulation of the kinetics of oxygen complexes in crystalline silicon. *Phys. Rev. B*, 66(16):165221, 2002.

[20] Joo Lee Young et al. Aggregation kinetics of thermal double donors in silicon. *Phys. Rev. Lett.*, 86(14):3060–3063, 2001.

[21] J. Härkönen et al. (incl. E. Tuovinen). Processing microstrip detectors on Czochralski grown silicon. *Nucl. Instrum. Methods Phys. Res., Sect. A*, 514:173–179, 2003.

[22] J. Härkönen et al. (incl. E. Tuovinen). Particle detectors made of high-resistivity Czochralski silicon. *Phys. Scr. T.*, 114:88–90, 2004.

[23] Helsinki University of Technology Micro and Nanofabrication Center, `http://www.micronova.fi/units/minfab/`.

[24] R.C. Newman. Light impurities and their interaction in silicon. *Mater. Sci. Eng. B*, 36:1–12, 1996.

[25] E. Simoen et al. Hydrogen plasma-enhanced thermal donor formation in n-type oxygen-doped high-resistivity float-zone silicon. *Appl. Phys. Lett.*, 81(10):1842–1844, 2002.

[26] R. Job et al. Hydrogen enhanced thermal donor formation in oxygen enriched high resistive float-zone silicon. *Nucl. Instrum. Methods Phys. Res., Sect. B*, 186:116–120, 2002.

[27] Stopping range of ions in matter-simulation program, `http://www.srim.org/`.

[28] D.K. Schroder. *Semiconductor material and device characterization*. John Wiley & sons, 2nd edition, 1998.

[29] G. Lindström. Radiation damage in silicon detectors. *Nucl. Instrum. Methods Phys. Res., Sect. A*, 512:30–43, 2003.

[30] ASTM E722-85, ASTM E722-93 (revised), 1993.

[31] M. Huhtinen. Simulation of non-ionizing energy loss and defect formation in silicon. *Nucl. Instrum. Methods Phys. Res., Sect. A*, 491:194–215, 2002.

[32] Shahyar Saramad and Ali Moussavi Zarandi. The bulk damaged effects of clustered defects in irradiated silicon detectors. *Phys. B*, 273-274:1041–1044, 1999.

[33] M. Laakso, P.Singh, and P.F. Shepard. Field oxide radiation damage measurements in silicon strip detectors. *Nucl. Instrum. Methods Phys. Res., Sect. A*, 327:517–522, 1993.

[34] M. Moll et al. Leakage current of hadron irradiated silicon detectors – material dependence. *Nucl. Instrum. Methods Phys. Res., Sect. A*, 426:87–93, 1999.

[35] M. Moll. *Radiation damage in silicon particle detectors – microscopic defects and macroscopic properties*. PhD thesis, Hamburg University, 1999. ISSN-1435-8085.

[36] G. Kramberger et al. Effective trapping time of electrons and holes in different materials irradiated with neutrons and protons and pions. *Nucl. Instrum. Methods Phys. Res., Sect. A*, 481:297–305, 2002.

[37] I. Lazanu and S. Lazanu. Annealing of radiation-induced defects in silicon in a simplified phenomenological model. *Nucl. Instrum. Methods Phys. Res., Sect. B*, 183:383–390, 2001.

[38] P. Luukka et al. (incl. E. Tuovinen). Test beam results of a proton irradiated Czochralski silicon strip detector. *Nucl. Instrum. Methods Phys. Res., Sect. A*, 530:117–121, 2004.

[39] Z. Li et al. (incl. E. Tuovinen). Radiation hardness of high resistivity magnetic Czochralski silicon detectors. *IEEE Trans. Nucl. Sci.*, 51(4):1901–1908, 2004.

[40] Z. Li et al. (incl. E. Tuovinen). Gamma radiation induced space charge sign inversion and re-inversion in p-type mcz si detectors and in proton-irradiated n-type mcz si detectors. *Nucl. Instrum. Methods Phys. Res., Sect. A*, 552:34–42, 2005.

[41] G. Kramberger and D. Contarato. How to achieve highest charge collection efficiency in heavily irradiated position-sensitive silicon detector. *Nucl. Instrum. Methods Phys. Res., Sect. A*, 560:98–102, 2006.

[42] V. Eremin et al. Development of transient current and charge techniques for the measurement of effective net concentration of ionized charged (n_eff) in the space charge region of p-n junction detectors. *Nucl. Instrum. Methods Phys. Res., Sect. A*, 372:388–398, 1996.

[43] T.J. Brodbeck et al. A new method of carrier trapping time measurement. *Nucl. Instrum. Methods Phys. Res., Sect. A*, 473:645, 2001.

[44] G. Kramberger et al. Determination of effective trapping times fer electrons and holes in irradiated silicon. *Nucl. Instrum. Methods Phys. Res., Sect. A*, 476:645–651, 2002.

Appendix A

Full process flow

1. Ion implantation (Contact at the back)
   Back: Phosphorus 70 keV dose 10^{15} cm^{-2}

2. RCA-clean
   10 min in 5:1:1 H_2O:NH_2:H_2O_2 at 80°C + rinse
   15 min in 5:1:1 H_2O:HCl:H_2O_2 at 80°C + rinse
   20 s in 50:1 H_2O:HF + Rinse
   Drying in a centrifuge

3. Dry oxidation
   Load-in at 700°C
   Stabilization 10 min
   Ramp-up 10°C/min
   Stabilization 10 min, 1100°C
   Dryox 300 min, 1100°C
   Anneal 30 min, 1100°C
   Ramp-down 4°C/min
   Unload at 700°C

4. Lithography (Alignment marks)
   10 min bake at 120°C
   HMDS in vacuum exicator 5 min
   Resist spinning AZ5214E
   15 min pre-bake at 90°C
   Exposure 2.0 s Karl Süss MA-6
   Development 40 s in AZ351B
   20 min post-bake at 120°C

5. RIE etching
   SiO_2: 9 min with CHF_3:O_2, 50 sccm: 5 sccm, press = 55 mTorr, P = 150 W
   Si: 1 min with SF_6, 100 sccm, press = 30 mTorr, P = 100 W

6. Resist removal
   10 min in acetone with ultrasound
   5 min in clean acetone
   5 min in iso-propanol
   Rinsing
   Drying in centrifuge

7. Lithography (Implantation opening)

8. BHF SioEtch
   BHF SioEtch 165 s at 31°C
   Rinsing
   Drying in centrifuge

9. Resist removal

10. Ion implantation (Strip implant)
    Front: Boron 30 keV dose 10^{15} cm^{-2}

11. BHF SioEtch 180 s at 31°C

12. RCA clean

13. Dry oxidation 100 nm
    As in 3., except oxidation time is 46 min

14. WNx sputtering approx 60 nm
    Dynamic mode, rotation 6 1/min, time = 200 s
    flow(Ar) = 100, flow(N_2) = 30, P_{DC} = 600 W, press = 6 mTorr

15. Aluminum adhesion layer 1 min Dynamic mode, rotation 6 1/min
    flow(Ar) = 70 sccm, P_{DC} = 2000 W, pres = 4 mTorr

16. Lithography (Bias resistors)

17. Aluminum etching in phosphoric acid etchant (80-16-04 phosphoric acid - acetic acid - nitric acid)
    60 s at room temperature

18. WN_x etching with RIE
    WN_x: 3 min with CHF_3:Ar, 25 sccm : 25 sccm, P = 200 W and press = 30 mTorr

19. WN_x etching with 1:1 H_2O_2:H_2O, 45 minutes
20. Resist removal and adhesion layer removal
21. Lithography (Contact opening)
22. BHF SioEtch 60 s at 31°C
23. Resist removal
24. Aluminum sputtering approx. 500nm
    Dynamic mode, rotation 6 1/min
    flow(Ar) = 70 sccm, P_{DC} = 2000 W, pres = 4 mTorr
25. Lithography (Metallization)
26. Aluminum etching in phosphoric acid etchant (80-16-04 phosphoric acid - acetic acid - nitric acid)
    50 s at 80°C
27. Resist removal
28. Aluminum sputtering on the backside approx. 500 nm
    Dynamic mode rotation 6 1/min
    flow(Ar) = 70 sccm, P_{DC} = 2000 W, pres = 4 mTorr
29. Sintering
    370°C for TD sensitive materials
    430°C or 450°C for intentional TD creation
30. PECVD passivation
    100 nm SiN_x and 100 nm SiO_2 deposition done at 300°C
31. Lithography (Passivation opening)
32. RIE etching
    SiO_2: 2 min with CHF_3:O_2, 50 sccm : 5 sccm, P = 150 W and press = 55 mTorr
    SiN_x: 3 min with CHF_3:Ar, 25 sccm : 25 sccm, P = 200 W and press = 30 mTorr
33. Resist removal
34. Process end wafers to dicing

List of Symbols

A	area of the diode
C	capacitance per unit-area
C_{geo}	geometrical capacitance
CCE	charge-collection effciency
CCE_{geom}	geometrical term in charge-collection efficiency
CCE_{trap}	trapping term in charge-collection efficiency
D	diffusion coefficient,
	displacement damage cross-section
D_i	diffusion coefficient for interstitial oxygen
D_n	diffusion coefficient for electrons,
	displacement damage cross-section for 1 MeV neutrons
D_p	diffusion coefficient for holes
$D_{particle}$	displacement damage cross-section for given particle
d	thickness of the diode
E	electric field
E_A	activation energy
E_B	critical value for the electric field
E_{max}	maximum of the electric field
J_{gen}	generation current density
J_R	recombination current density
J_S	current density given by Shockley equation
k	Bolzmann's constant
L_p	diffusion length for holes
L_n	diffusion length for electrons
N_A	acceptor atom density
N_D	donor atom density
N_B	doping density of the lightly doped bulk material
N_{TD}	thermal donor density
n_i	intrinsic charge carrier concentration

n_{p0}	minority-carrier density in p-region
O_i	concentration of interstitial oxygen
p_{n0}	minority-carrier density in n-region
q	absolute value of the electron charge
Q_{coll}	collected charge
Q_{ref}	collected charge from a reference detector
s_r	surface recombination velocity
T	absolute temperature
t	time
vol	active volume
V_B	breakdown voltage
V_{bi}	built-in potential
V_{dep}	depletion voltage
V_{ext}	external bias voltage
V_{fd}	full-depletion voltage
W, w	width of the depletion region
α	current-related damage rate
ϵ_s	permittivity of semiconductor
ϕ	electric potential
χ	reaction order
κ	hardness factor
ρ	space-charge density
Φ_{eq}	1 MeV neutron equivalent fluence
τ_B	bulk lifetime
τ_{eff}	effective lifetime
τ_G	generation lifetime
τ_{trap}	trapping time

List of Abbreviations

ASTM	American Society for Testing and Materials
BHF	buffered hydro fluoric acid
CCE	charge-collection efficiency
CERN	European organization for nuclear research
CHF_3	trifluoromethane
CMS	compact muon solenoid
CV	capacitance-voltage
Cz	Czochralski
Cz-Si	Czochralski silicon
DOFZ	diffusion-oxygenated float-zone silicon
EGS	electronic grade polysilicon
ehp	electron-hole pair
FDS	fast-diffusing species
FZ	float-zone
FZ-Si	float-zone silicon
HEP	high-energy physics
H_2O_2	hydrogen peroxide
HV	high-voltage
ICECREM	a simulation program for processing steps in semiconductor production
ICP-RIE	inductively coupled plasma reactive ion etcher
IR	infrared
IV	current-voltage
LHC	large hadron collider
MCz	magnetic Czochralski
MCz-Si	magnetic Czochralski silicon
MINFAB	Micro and Nanofabrication Center
mip	minimum ionizing particle
NIEL	non-ionizing energy loss

O2	oxygen dimer
O_2	oxygen molecule
O3	oxygen trimer
PCD	photoconductivity decay
PECVD	plasma-enhanced chemical vapor deposition
QV	charge-voltage
RCA	Radio Corporation of America
RD39	CERN collaboration: Cryogenic Tracking Detectors
RD48	CERN collaboration: Radiation Hardening of Silicon Detectors (ROSE)
RD50	CERN collaboration: Radiation hard semiconductor devices for very high-luminosity colliders
RIE	reactive ion etcher
SCSI	space charge sign inversion
SEM	scanning electron microscope
SiC	silicon carbide
SiO_2	silicon dioxide
SMU	source meter unit
SNR	signal-to-noise ratio
SRIM	stopping range in matter (simulation program)
TCT	transient current technique
TD	thermal donor
TKK	Helsinki University of Technology
V-O	vacancy-oxygen pair
V_2O	divacancy oxygen complex
V_2	divacancy
WN_x	tungsten nitride (unknown composition)
μPCD	microwave-detected photoconductivity decay